J. Fluid Mech. (2024), *vol*. 980, A12, doi:10.1017/jfm.2023.1073

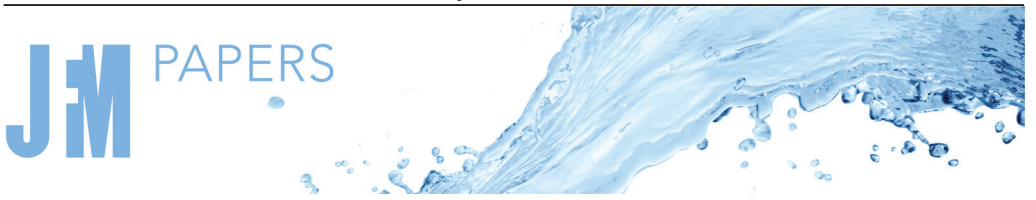

A data-driven quasi-linear approximation for turbulent channel flow

Jacob J. Holford[1],†, **Myoungkyu Lee**[2] **and Yongyun Hwang**[1]

[1]Department of Aeronautics, Imperial College London, South Kensington, London SW7 2AZ, UK

[2]Department of Mechanical Engineering, University of Houston, Houston, TX 77204, USA

(Received 19 May 2023; revised 29 September 2023; accepted 16 November 2023)

A data-driven implementation of a quasi-linear approximation is presented, extending a minimal quasi-linear approximation (MQLA) (Hwang & Ekchardt, *J. Fluid Mech.*, vol. 894, 2020, p. A23) to incorporate non-zero streamwise Fourier modes. A data-based approach is proposed, matching the two-dimensional wavenumber spectra for a fixed spanwise wavenumber between a direct numerical simulation (DNS) (Lee & Moser, *J. Fluid Mech.*, vol. 774, 2015, pp. 395–415) and that generated by the eddy viscosity enhanced linearised Navier–Stokes equations at $Re_\tau \approx 5200$, where Re_τ is the friction Reynolds number. Leveraging the self-similar nature of the energy-containing part in the DNS velocity spectra, a universal self-similar streamwise wavenumber weight is determined for the linearised fluctuation equations at $Re_\tau \simeq 5200$. The data-driven quasi-linear approximation (DQLA) provides noteworthy enhancements in the wall-normal and spanwise turbulence intensity profiles. It exhibits a qualitatively similar structure in the spanwise wavenumber velocity spectra compared with the MQLA. Additionally, the DQLA offers extra statistical outputs in the streamwise wavenumber coordinates, enabling a comprehensive global analysis of this modelling approach. By comparing the DQLA results with DNS results, the limitations of the presented framework are discussed, mainly pertaining to the lack of the streak instability (or transient growth) mechanism and energy cascade from the linearised model. The DQLA is subsequently employed over a range of Reynolds numbers up to $Re_\tau = 10^5$. Overall, the turbulence statistics and spectra produced by the DQLA scale consistently with the available DNS and experimental data, with the Townsend–Perry constants displaying a mild Reynolds dependence (Hwang, Hutchins & Marusic, *J. Fluid Mech.*, vol. 933, 2022, p. A8). The scaling behaviour of the turbulence intensity profiles deviates away from the classic $\ln(Re_\tau)$ scaling, following the inverse centreline velocity scaling for the higher Reynolds numbers.

Key words: turbulence modelling, turbulence theory, low-dimensional models

† Email address for correspondence: jh5315@ic.ac.uk

© The Author(s), 2024. Published by Cambridge University Press

https://doi.org/10.1017/jfm.2023.1073 Published online by Cambridge University Press

1. Introduction

Recently, an increasingly popular approach in modelling turbulent flows is the use of the linearised Navier–Stokes equations. For example, the linearised Navier–Stokes equations are used: (i) to understand the origin of coherent structures (del Álamo & Jiménez 2006; Hwang & Cossu 2010; McKeon & Sharma 2010); (ii) to generate statistical inputs for the state-space estimation problem (Illingworth, Monty & Marusic 2018; Madhusudanan, Illingworth & Marusic 2019; Morra *et al.* 2019; Gupta *et al.* 2021); (iii) for a predictive quasi-linear approximation (Hwang & Eckhardt 2020; Skouloudis & Hwang 2021); (iv) to produce a reduced-order description of exact coherent states and turbulence statistics in the minimal flow unit (Rosenberg & McKeon 2019; Nogueira *et al.* 2020); (v) for statistics completion problems from partial measurements (Zare, Jovanović & Georgiou 2017; Towne, Lozano-Durán & Yang 2019); (vi) to produce reduced-order models for existing flow control strategies (Luhar, Sharma & McKeon 2014; Ran, Zare & Jovanović 2021). In wall-bounded turbulent flows, an essential feature in modelling the fluctuating state is how the nonlinear term is replaced. Since wall-bounded turbulent flows are linearly stable (Butler & Farrell 1993; Pujals *et al.* 2009), a forcing or driving term is necessary to generate non-trivial solutions. Since this forcing term directly replaces the nonlinearity, how accurately this forcing statistically mimics the physics of the nonlinearity has also been observed as a key to the performance of linear models in their various uses (Gupta *et al.* 2021; Morra *et al.* 2021; Symon *et al.* 2022).

One such modelling framework, which leveraged 'predictive' features of the physics of wall-bounded shear flows, was recently proposed by Hwang & Eckhardt (2020). In this approach, referred to as minimal quasi-linear approximation (MQLA), the attached eddy model of Townsend (1976) was revisited to relax the inviscid limit, allowing statistics to be predicted for high yet finite Reynolds numbers. The MQLA achieved this by following the framework of a quasi-linear approximation. The general idea of this approach is to decompose the velocity state into two separate groups, typically a large- and small-scale state. An approximation then arises when the nonlinear self-interactions of the small-scale state are neglected, and instead, a closure is provided. The earliest works that implemented a quasi-linear approximation (Malkus 1954, 1956; Herring 1963, 1964, 1966) provided a closure through a marginal stability criterion. The linear stability of wall-bounded turbulence means that alternative closures have to be provided. Indeed, in modern variants of quasi-linear approximations, the nonlinear self-interactions of the small-scale state have been more flexibly modelled, depending on the nature of the flow and the purpose of the approximation. Such examples include stochastic structural stability theory (Farrell & Ioannou 2007, 2012), direct statistical simulation (Marston, Conover & Schneider 2008; Tobias & Marston 2013), self-consistent approximations (Mantič-Lugo, Arratia & Gallaire 2014; Mantič-Lugo & Gallaire 2016), restricted nonlinear models (Thomas *et al.* 2014, 2015; Farrell *et al.* 2016), a quasi-linear approximation applied to exact coherent states (Hall & Sherwin 2010; Pausch *et al.* 2019) and generalised quasi-linear approximations (Marston, Chini & Tobias 2016; Tobias & Marston 2017; Hernández, Yang & Hwang 2022*a*). The MQLA provided a closure through a stochastic forcing term, implemented self-consistently, i.e. the self-interactions of the small-scale state were enforced to be consistent with the large-scale state, in this case, the mean profile.

From the perspective of the attached eddy hypothesis, the MQLA can be regarded as a controlled approximation with the eddies arising from the linearised Navier–Stokes equations. These linear solutions replace the assumed statistical structure of the representative energy-containing eddies used by Townsend, Perry and co-workers (Townsend 1976; Perry & Chong 1982; Perry, Henbest & Chong 1986). The solutions of

https://doi.org/10.1017/jfm.2023.1073 Published online by Cambridge University Press

the linearised Navier–Stokes equations used in the MQLA have the advantage of closely resembling a stage of the self-sustaining process (Hamilton, Kim & Waleffe 1995; Waleffe 1997), a cycle ubiquitous in wall-bounded shear flows and the proposed mechanism for which each of the energy-containing eddies can be sustained (Hwang 2015). In this linear portion of the self-sustaining process, streamwise vortices drive the formation of elongated streaks (i.e. the lift-up effect) (Ellingsen & Palm 1975; Schmid & Henningson 2001; Brandt 2014), the key length scales of which are determined through the eddy viscosity enhanced linearised Navier–Stokes operator (Hwang & Cossu 2010). Instead of superposing the representative statistical structure of the energy-containing eddies subject to constant Reynolds shear stress, as done by Townsend (1976), the nonlinear term in the linearised fluctuation equations was replaced self-consistently. The linear operator was modified by an eddy viscosity diffusion term and a forcing structure that generates the Reynolds shear stress identical to that from the nonlinear mean equation. In other words, a self-consistent closure of a quasi-linear approximation was provided. With the mean profile known, the MQLA becomes a predictive framework. The forcing term required to drive the Reynolds shear stress consistent with the mean profile allows further statistics of the velocity fluctuations to be determined at different Reynolds numbers.

Although the attached eddy hypothesis assumes and leverages the self-similar nature of the eddies, attention has been turned to understanding the statistical structure of the forcing or nonlinear term. The benefits of having a well-prescribed model for the nonlinear term are demonstrated, for example, by the performance of state-space estimators (Hœpffner *et al.* 2005; Chevalier *et al.* 2006; Illingworth *et al.* 2018; Madhusudanan *et al.* 2019; Morra *et al.* 2019), with more physical models for the nonlinear term resulting in better predictions of velocity statistics across the wall-normal direction (Gupta *et al.* 2021). There is a variety of approaches in determining and modelling the forcing term, ranging from statistically exact control and optimisation-based techniques (for a review, see Jovanović 2021) to measurement through direct numerical simulation (Chevalier *et al.* 2006; Nogueira *et al.* 2020; Morra *et al.* 2021), as well as more phenomenological modelling (Jovanović & Bamieh 2001; Gupta *et al.* 2021; Holford, Lee & Hwang 2023). For example, Zare *et al.* (2017) determined a set of two-point coloured-in-time forcing statistics through an optimisation problem. This optimisation problem had constraints such that the velocity spectral density exactly matched that of a direct numerical simulation (DNS). This work was recently complemented by Abootorabi & Zare (2023), which demonstrated the benefits of an additional eddy viscosity diffusion operator to the coloured-in-time forcing. While these methods can yield forcing statistics that generate the exact velocity statistics, often, the techniques are local in the sense that they are applied to a single wavenumber pair and hence have to be repeated for every wavenumber pair to build a global forcing structure.

Regarding implementing a predictive framework, the inputs to many models are often obtained through DNS, which is frequently a desirable output. To address this issue, Holford *et al.* (2023) recently identified a global forcing structure across the entire wavenumbers required for the eddy viscosity enhanced linearised Navier–Stokes operator with a simplification that the forcing is white in time and decorrelated in space. The findings revealed the self-similar nature of the forcing spectra corresponding to the main energy-containing part of the velocity spectra. In the current work, Holford *et al.* (2023) is approximately followed to provide a global structure for the forcing across streamwise wavenumbers and Reynolds numbers.

The main findings of the MQLA (Hwang & Eckhardt 2020) were consistent with the seminal predictions of Townsend's attached eddy hypothesis on turbulence intensities. By superposing the solutions of the linearised Navier–Stokes equations with a forcing that

https://doi.org/10.1017/jfm.2023.1073 Published online by Cambridge University Press

provides a self-consistent Reynolds shear stress, a logarithmic decay in the wall-parallel turbulence intensities was found, as well as a region where the wall-normal turbulence intensity is approximately constant. Additionally, since the determination of the fluctuating velocity generated Reynolds shear stress in the MQLA requires integration of the velocity spectra, the scaling behaviour of the one-dimensional velocity spectra could also be extrapolated to exceptionally high Reynolds numbers (Skouloudis & Hwang 2021). A strong qualitative match was found between the one-dimensional spanwise wavenumber velocity spectra produced by the MQLA and those reported by DNS (Lee & Moser 2015). However, important quantitative differences were also found. In particular, turbulence intensities of the MQLA were highly anisotropic compared with those of DNS, with the streamwise turbulence intensity far exceeding that of DNS. At the same time, the other velocity components, particularly the wall-normal component, were significantly lower. This result stems from neglecting the streamwise varying Fourier modes in the MQLA, causing the absence of streamwise pressure strain that transfers the energy produced in the streamwise component to the other components (Cho, Hwang & Choi 2018; Lee & Moser 2019). Neglecting the streamwise varying Fourier modes is also understood to prohibit the MQLA's capabilities in reproducing features of the self-sustaining process beyond the lift-up effect, particularly the streak instability or transient growth, which plays a crucial role in redistributing turbulent kinetic energy from the streamwise velocity component to the others (Schoppa & Hussain 2002; de Giovanetti, Sung & Hwang 2017; Doohan, Willis & Hwang 2021; Lozano-Durán *et al.* 2021).

The present paper aims to extend the MQLA to include the streamwise varying Fourier modes, with an emphasis on maintaining the predictive nature of the MQLA at different Reynolds numbers. To this end, a physics-aware data-driven approach will be taken. Hereafter, the framework of the current study will be referred to as the data-driven quasi-linear approximation (DQLA) to distinguish it from the MQLA. The DQLA framework incorporates the physics element through the attached eddy hypothesis and enforces self-similarity of the forcing with respect to the spanwise length scale. The detailed structure of the forcing is determined using the DNS database from Lee & Moser (2015). This approach relies on the self-similar nature of the eddy viscosity enhanced linear operator (Hwang & Cossu 2010), which has been corroborated by recent findings on the statistical structure of the forcing of this linear model from Holford *et al.* (2023). While developing a predictive model for turbulent statistics and spectra, the DQLA will provide a fair means of evaluating the performance of the eddy viscosity diffusion operator within linear modelling frameworks. In particular, by incorporating non-zero streamwise wavenumbers, it allows for a comprehensive assessment across a wide range of wavenumber pairs. The results presented represent an initial step, focusing on the evaluation of velocity spectra.

The paper is organised as follows. The DQLA framework is developed in § 2, formulating two optimisation problems. Firstly a self-similar weight is determined following Holford *et al.* (2023). This weight is then extrapolated across all considered Fourier modes, and a quasi-linear approximation is then implemented following Hwang & Eckhardt (2020). The linear model used throughout this study includes an eddy viscosity diffusion operator, and its significance is briefly discussed. The results of the DQLA at $Re_\tau \simeq 5200$, where Re_τ is the friction Reynolds number, are then compared with statistics from DNS of Lee & Moser (2015) in § 3. Emphasis will be placed on the streamwise one-dimensional and two-dimensional velocity spectra since the MQLA cannot produce these statistics. Additionally, any quantitative improvements of the DQLA compared with the MQLA will be discussed concerning the inclusion of streamwise varying Fourier modes. The predictive capabilities of the DQLA will be assessed by extrapolating results

https://doi.org/10.1017/jfm.2023.1073 Published online by Cambridge University Press

up to $Re_\tau = 10^5$ in § 4. The paper is then concluded in § 5, which summarises the results and limitations of this framework.

2. Problem formulation

2.1. *Turbulent channel flow*

A quasi-linear approximation for incompressible, fully developed turbulent channel flow is considered. The flow domain is the region confined between two infinitely long and wide plates. The coordinates along the streamwise, wall-normal and spanwise directions are denoted by x, y and z, respectively, with a corresponding velocity vector $\boldsymbol{u} = (u,\ v,\ w)$. The two plates are located at $y = 0, 2h$, where h represents the half-width of the channel. The velocity field is decomposed into a time-averaged mean field, $\boldsymbol{U} = (U(y),\ 0,\ 0)$, and the fluctuating velocity about this mean profile, $\boldsymbol{u}' = (u',\ v',\ w')$, i.e. the Reynolds decomposition. This results in the following coupled set of equations:

$$\nu \frac{\mathrm{d}U}{\mathrm{d}y} - \overline{u'v'} = \frac{\tau_w}{\rho}\left(1 - \frac{y}{h}\right), \tag{2.1a}$$

$$\frac{\partial \boldsymbol{u}'}{\partial t} + (\boldsymbol{U}\cdot\boldsymbol{\nabla})\boldsymbol{u}' + (\boldsymbol{u}'\cdot\boldsymbol{\nabla})\boldsymbol{U} = -\frac{1}{\rho}\boldsymbol{\nabla} p + \nu\boldsymbol{\nabla}^2\boldsymbol{u} + \boldsymbol{N}, \tag{2.1b}$$

where

$$\mathcal{N} = -\boldsymbol{\nabla}\cdot(\boldsymbol{u}'\boldsymbol{u}' - \overline{\boldsymbol{u}'\boldsymbol{u}'}). \tag{2.1c}$$

Here, t denotes time, ρ the fluid density, p' the fluctuating pressure, ν the kinematic viscosity, $\overline{(\cdot)}$ a time-averaged quantity and τ_w is the time-averaged wall shear stress. Following the typical quasi-linear approximation framework, the time-averaged mean profile equation retains this form, including the nonlinear Reynolds shear stress term feeding back from the fluctuating velocity field. The dynamics of the fluctuating velocity is then 'linearised,' dropping the self-advection term.

As the associated linear operator is stable for the turbulent mean profile in channel flow (Pujals *et al.* 2009), an additional driving term must be considered for non-trivial statistics. To this end, the nonlinear term is replaced with the following model:

$$\mathcal{N}_{\nu_t,f} = \boldsymbol{\nabla}\cdot(\nu_t(\boldsymbol{\nabla}\boldsymbol{u}' + \boldsymbol{\nabla}\boldsymbol{u}'^T)) + \boldsymbol{f}', \tag{2.2a}$$

where $\boldsymbol{f}' = (f'_u, f'_v, f'_w)$ is a stochastic forcing term and Cess' expression (Cess 1958) is used for the eddy viscosity profile

$$\nu_t(\eta) = \frac{\nu}{2}\left\{1 + \frac{\kappa^2 Re_\tau^2}{9}(1-\eta^2)^2(1+2\eta^2)^2(1-\exp[(|\eta|-1)Re_\tau/A])^2\right\}^{0.5} - \frac{\nu}{2}, \tag{2.2b}$$

with $\eta = (y-h)/h$. Including the eddy viscosity term in (2.2*a*) is not a necessity. Using only a forcing term would leave the coupled system as statistically 'exact' if the forcing was set to be identical to a set of known statistics generated by the nonlinear term. That being said, the covariance of the nonlinear term has been demonstrated to not possess sign definiteness (Zare *et al.* 2017), which significantly complicates the modelling procedure (for example, Zare *et al.* 2017). The advantage of using the eddy viscosity modified operator lies in the relaxation of this complication with a physical model, although its use does not necessarily enforce the energy neutrality of the nonlinear term. By doing so, the forcing input can be kept as white in time, whereas the overall model for the nonlinear

https://doi.org/10.1017/jfm.2023.1073 Published online by Cambridge University Press

term will be coloured in time through the eddy viscosity. It has been demonstrated that this eddy viscosity term phenomenologically mimics some features of the nonlinear term, including the removal of energy across all integral length scales (Symon, Illingworth & Marusic 2021), as well as the modelling of the wall-attached footprints of large scales in the velocity spectra of the wall-parallel components (Symon *et al.* 2022; Holford *et al.* 2023). The same eddy viscosity is also used as a closure in determining the mean velocity profile with

$$-\overline{u'v'} = \nu_t \frac{\mathrm{d}U}{\mathrm{d}y}, \tag{2.3}$$

upon which solving (2.1*a*) gives the robust law of the wall. Following this closure for the mean profile, the eddy viscosity parameters are set with $\kappa = 0.426$ and $A = 25.4$, obtained by the best least squares fitting of the mean profile obtained by integrating (2.1*a*) with (2.3) and the DNS mean profile at $Re_\tau \approx 2000$ (del Álamo & Jiménez 2006). The crude physical argument for using the same eddy viscosity profile in the mean and fluctuating velocity component equates to both velocity fields experiencing the same background turbulence. Although this physical assumption is used mainly for simplicity, the inclusion of an eddy viscosity diffusion operator has been shown to be beneficial in many previous studies (see, for example, Pujals *et al.* 2009; Zare *et al.* 2017; Illingworth *et al.* 2018; Morra *et al.* 2019; Symon *et al.* 2021). Notably, the inclusion of the eddy-viscosity-based diffusion enables one to describe the inner-scaling behaviour of the near-wall-attached region of the outer-scale structures observed in full DNS, in terms of the modes associated with transient growth, resolvent analysis and the stochastic response of the linearised fluctuation equations (Hwang & Cossu 2010; Hwang 2016).

In the present study, the forcing is first considered to be white in time and decorrelated in the wall-normal direction for the purpose of utilising the framework of the stochastic linear dynamical system (Farrell & Ioannou 1992; Jovanović & Bamieh 2005; Hwang & Cossu 2010). Given the homogeneous nature of the wall-parallel directions, it is convenient to consider the Fourier transform along those directions

$$\hat{\boldsymbol{f}}'(t, y; k_x, k_z) = \int_{-\infty}^{\infty}\int_{-\infty}^{\infty} \boldsymbol{f}'(t, x, y, z)\exp(\mathrm{i}(k_x x + k_z z))\,\mathrm{d}x\,\mathrm{d}z, \tag{2.4}$$

giving the wall-normal forcing profiles at a given pair of streamwise and spanwise length scales $\lambda_x = 2\pi/k_x$ and $\lambda_z = 2\pi/k_z$, where (k_x, k_z) is the considered wavenumber pair. Analogous definitions of the Fourier transform are used for the other flow states. The spectral covariance matrix for the forcing is then considered to be

$$\begin{aligned}&\mathbb{E}[\hat{\boldsymbol{f}}'(y, t; k_x, k_z)\hat{\boldsymbol{f}}'^{H}(y', t'; k_x, k_z)] \\ &\quad = \begin{bmatrix} W_u(k_x, k_z) & 0 & 0 \\ 0 & W_v(k_x, k_z) & 0 \\ 0 & 0 & W_w(k_x, k_z) \end{bmatrix} \delta(y - y')\delta(t - t'),\end{aligned} \tag{2.5}$$

where $(\cdot)^H$ denotes complex conjugate transpose, $\mathbb{E}[\cdot]$ is the expectation operator over different stochastic realisations and W_r, with $r = \{u, v, w\}$, are componentwise weights to be determined. Here, the forcing amplitude is considered to vary componentwise, and this is to model the anisotropic nature of the velocity statistics and spectra in channel flow more flexibly.

https://doi.org/10.1017/jfm.2023.1073 Published online by Cambridge University Press

Re_τ	N_y	N_{k_x}	N_{k_z}	γ	$\|\overline{u'v'} - \mathbb{E}[u'v']\|_Q^2$	$\|\overline{u'v'} - \mathbb{E}[u'v']\|_{L_2}^2$
500	128	172	126	1.0×10^{-4}	4.91×10^{-4}	3.03×10^{-5}
1000	256	186	140	5.0×10^{-5}	6.17×10^{-4}	3.12×10^{-5}
2000	256	200	154	9.0×10^{-5}	7.30×10^{-4}	3.54×10^{-5}
5200	384	219	173	2.0×10^{-4}	7.92×10^{-4}	3.24×10^{-5}
10 000	512	232	186	1.0×10^{-4}	7.98×10^{-4}	3.12×10^{-5}
20 000	768	246	200	7.5×10^{-4}	7.83×10^{-4}	2.97×10^{-5}
50 000	1024	264	218	1.5×10^{-4}	8.53×10^{-4}	3.82×10^{-5}
100 000	1536	278	232	9.0×10^{-5}	9.57×10^{-4}	2.04×10^{-5}

Table 1. Numerical and optimisation parameters used in the present study: N_{k_x}, the number of streamwise wavenumbers; N_{k_z}, the number of spanwise wavenumbers; N_y, the number of wall-normal collocation points.

The resulting power- and cross-spectral densities of velocity fluctuations are obtained from the following velocity spectral covariance matrix:

$$\boldsymbol{\Phi_{uu}}(y, y'; k_x, k_z) = \mathbb{E}[\hat{\boldsymbol{u}}'(y, t; k_x, k_z)\hat{\boldsymbol{u}}'^H(y', t; k_x, k_z)]. \tag{2.6a}$$

Given the linear relation between the velocity and forcing spectral covariance matrices (Farrell & Ioannou 1992; Jovanović & Bamieh 2005; Hwang & Cossu 2010), $\boldsymbol{\Phi_{uu}}(y, y'; k_x, k_z)$ can further be decomposed into

$$\boldsymbol{\Phi_{uu}}(y, y'; k_x, k_z) = \sum_{r=u,v,w} W_r(k_x, k_z)\boldsymbol{\Phi_{uu,r}}(y, y'; k_x, k_z), \tag{2.6b}$$

where $\boldsymbol{\Phi_{uu,r}}(y, y'; k_x, k_z)$ is the velocity spectral covariance matrix associated with each component of the forcing with the unit amplitude: for example, $\boldsymbol{\Phi_{uu,u}}$ is obtained by setting the forcing spectral covariance to be

$$\mathbb{E}[\hat{\boldsymbol{f}}'(y, t; k_x, k_z)\hat{\boldsymbol{f}}'^H(y', t'; k_x, k_z)] = \begin{bmatrix} \delta(y - y') & 0 & 0 \\ 0 & 0 & 0 \\ 0 & 0 & 0 \end{bmatrix} \delta(t - t'), \tag{2.7}$$

and $\boldsymbol{\Phi_{uu,v}}$ and $\boldsymbol{\Phi_{uu,w}}$ are obtained in the same manner. In this study, $\boldsymbol{\Phi_{uu,r}}$ for $r = \{u, v, w\}$ are obtained by solving the standard Lyapunov equation formulated with the Orr–Sommerfeld–Squire system of equations. The equations are discretised using a Chebyshev collocation method (Weideman & Reddy 2000) with the wall-normal grid points reported in table 1. For the details of the solution method, the reader may refer to previous studies (Hwang & Cossu 2010; Holford *et al.* 2023). The domain of streamwise and spanwise wavelengths are considered as $(\lambda_x, \lambda_z) \in [10\delta_\nu, 10\delta_\nu] \times [100h, 10h]$ ($\delta_\nu = \nu/u_\tau$, where u_τ is the friction velocity) to cover a range of length scales including near-wall motions, as well as very large-scale motions in the outer region.

2.2. *Simplifications*

The forcing covariance considered in (2.5) may be a starting point of the proposed quasi-linear approximation. However, a white-in-time, uniform forcing in the wall-normal direction at each k_x and k_z is non-physical. In particular, a uniform wall-normal forcing variance profile yields an undesirable, large energetic response near the channel centreline (see figures 5 and 6 in Hwang & Eckhardt 2020). It was previously shown that considering

https://doi.org/10.1017/jfm.2023.1073 Published online by Cambridge University Press

some of the leading proper orthogonal decomposition (POD) modes from the response to this forcing offers an effective means to filter out these unwanted features, with respect to modelling the primary energy-containing motions at integral length scales (Hwang & Eckhardt 2020). That is not to say the less energetic POD modes are not useful – they may be useful in the modelling of other features of turbulence (e.g. small-scale spectra associated with energy cascade). This ansatz also exacerbates the anisotropy of the velocity fluctuations of the quasilinear models (see figure 5 in Hwang & Eckhardt 2020), although this is a necessary step to overcome the arbitrary assumption of a spatially white forcing input.

Given these previous experiences from Hwang & Eckhardt (2020), the forcing statistics in this study are also implicitly modified to drive leading POD modes that contain significant energetic content of the overall response (Hwang & Cossu 2010). Consequently, for a given wavenumber pair, the velocity spectral covariance matrix for each forcing component (i.e. $\boldsymbol{\Phi}_{\boldsymbol{uu},r}$) is further approximated in terms of the leading-order POD modes, such that

$$\boldsymbol{\Phi}_{\boldsymbol{uu},r}^{N_{POD}}(y,y';k_x,k_z)=\sum_{i=1}^{N_{POD}}\sigma_i\hat{\boldsymbol{u}}_{i,r,POD}(y;k_x,k_z)\hat{\boldsymbol{u}}_{i,r,POD}^{H}(y';k_x,k_z), \tag{2.8a}$$

where N_{POD} is the number of POD modes, and σ_i and $\hat{\boldsymbol{u}}_{i,r,POD}(y';k_x,k_z)$ are the eigenvalues and eigenfunctions of the original velocity spectral covariance matrix with white-in-time and spatially decorrelated forcing, denoted by $\boldsymbol{\Phi}_{\boldsymbol{uu}}^{W}$

$$\int_0^{2h}\boldsymbol{\Phi}_{\boldsymbol{uu}}^{W}(y,y';k_x,k_z)\hat{\boldsymbol{u}}_{i,POD}(y';k_x,k_z)\mathrm{d}y'=\sigma_i\hat{\boldsymbol{u}}_{i,POD}(y;k_x,k_z), \tag{2.8b}$$

with $\sigma_i\geq\sigma_{i+1}$. Considering the previous observation in Hwang & Eckhardt (2020), $N_{POD}=2$ is chosen here, retaining the most energetic structure when accounting for the geometrical symmetry in channel flow about $y=h$.

In addition to this, the weighting along the streamwise wavenumber axis is implemented considering the self-similarity of the forcing structure with respect to the spanwise wavenumber (Hwang & Cossu 2010; Holford *et al.* 2023), as expected from the attached eddy hypothesis of Townsend (Townsend 1976; Hwang 2015) (see § 2.3 for further details). Consequently, the weight of each component is decomposed into a part that retains the self-similar structure $W_{r,k_x}(k_x/k_z)$ along the streamwise wavenumber axis and a part that determines its amplitude $W_{k_z}(k_z)$ for each spanwise wavenumber, such that

$$W_r(k_x,k_z)=W_{r,k_x}(k_x/k_z)W_{k_z}(k_z), \tag{2.9}$$

giving the final form of velocity spectra covariance matrix for the quasi-linear approximation in this study

$$\boldsymbol{\Phi}_{\boldsymbol{uu}}(y,y';k_x,k_z)=W_{k_z}(k_z)\sum_{r=u,v,w}W_{r,k_x}(k_x/k_z)\boldsymbol{\Phi}_{\boldsymbol{uu},r}^{N_{POD}}(y,y';k_x,k_z). \tag{2.10}$$

The weights are determined by solving the optimisation problems proposed in the following two subsections.

2.3. *Data-driven determination of streamwise weighting*

To first determine the self-similar weight $W_{r,k_x}(k_x/k_z)$ along the streamwise wavenumber axis, for each k_z, an optimisation problem is considered such that (2.10) best matches

https://doi.org/10.1017/jfm.2023.1073 Published online by Cambridge University Press

the two-dimensional velocity spectra and Reynolds shear stress cospectra of DNS at $Re_\tau \approx 5200$ (Lee & Moser 2015), denoted by $\boldsymbol{\Phi}_{\boldsymbol{uu}}^{DNS}(y; k_x, k_z)$. This problem has recently been solved with the addition of a wall-normal variation in the forcing term in Holford *et al.* (2023), and the reader is referred to it for a more complete discussion on the modelling rationale. The present study leverages the main findings from Holford *et al.* (2023). However, a more straightforward problem is solved for the weight, with the use of the POD modes implicitly varying the wall-normal profile of the forcing term so that the modelling efforts can be extrapolated to other Reynolds numbers without using any further DNS data at different Reynolds numbers.

To determine the weight, two main observations are highlighted. The first is the self-similar nature of the velocity spectra from DNS with respect to the spanwise length scale (Hwang 2015; Holford *et al.* 2023). In particular, the self-similarity occurs at wavenumbers which contribute significantly to the turbulence intensity profiles, i.e. main energy-containing features of the spectra. The second is that the eddy viscosity modified linearised Navier–Stokes equations also generate an approximately self-similar response with respect to the spanwise length scale (Hwang & Cossu 2010; Hwang & Eckhardt 2020). Note that this second observation is primarily due to the eddy viscosity. The key feature of the eddy viscosity is $\nu_t \sim y$, responsible for the re-scaling property of the linear operator with respect to the spanwise wavenumber in the logarithmic region (Hwang & Cossu 2010). Combining these two observations, an optimisation problem that weights a self-similar linear response to an approximately self-similar set of DNS spectra is considered. It is then expected that the weights themselves would be self-similar, at least to the same degree as the DNS velocity spectra. A weighting is now determined to match the two-dimensional velocity spectra from DNS at a given spanwise length scale through the following optimisation problem:

$$\min_{W_{r,k_x}} \sum_s \frac{\|\boldsymbol{\Phi}_s^{DNS} - \boldsymbol{\Phi}_s(W_{r,k_x})\|_Q}{\|\boldsymbol{\Phi}_s^{DNS}\|_Q} + \sum_r \gamma J[W_{r,k_x}], \tag{2.11a}$$

subject to

$$W_{r,k_x}(k_x, y; k_z) \geq 0, \tag{2.11b}$$

where $r = \{u, v, w\}$, $s = \{uu, vv, ww, uv\}$ and γ is a parameter controlling the relative importance of the regularisation. Here, J is a regularisation functional to penalise the roughness of the forcing intensity, to ensure smooth velocity spectra and to partially denoise the DNS spectra (Holford *et al.* 2023), chosen to be

$$J[W_{r,k_x}] = \left\| \left(\frac{\partial^2 W_{r,k_x}}{\partial \ln {k_x}^2} \right) \right\|_Q, \tag{2.11c}$$

where $\|\cdot\|_Q$ is a norm defined as $\|\cdot\|_Q^2 = \int_0^{2h} \int_{-\infty}^{\infty} (\cdot)^2 k_x Q(y) \, \mathrm{d}\ln k_x \, \mathrm{d}y$ with weight $Q(y) = \chi^{-1}$, where $\chi = 1 - |\eta|$ is the distance from the wall, to place equal emphasis on points following a logarithmic scaling with distance from the wall. Note that the logarithmic coordinates are also used along the k_x-axis to focus the problem on the modelling of the self-similar energy-containing part, placing less significance on the non-self-similar part originating from energy cascade (see Holford *et al.* 2023, for a further discussion). In particular, the purpose of this weighting along the streamwise wavenumber axis is to provide a self-similar weight for use across all wavenumber pairs and all Reynolds numbers.

The convex optimisation problem (2.11) was solved by discretising the spectral velocity state onto $N_y = 512$ grid points with the Chebyshev collocation method.

https://doi.org/10.1017/jfm.2023.1073 Published online by Cambridge University Press

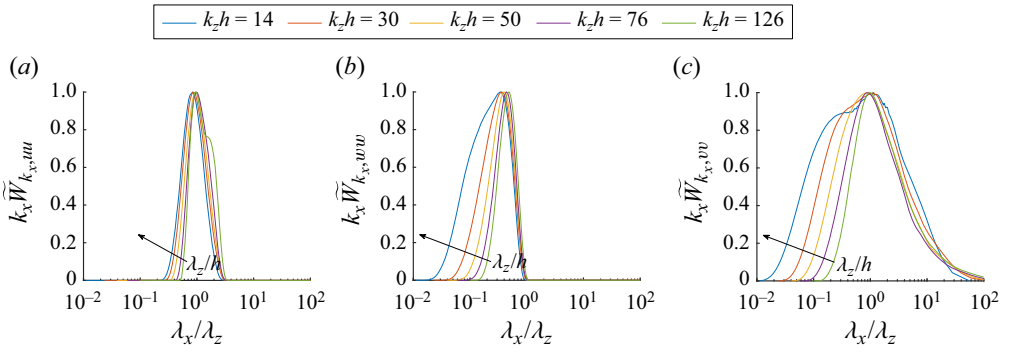

Figure 1. Premultiplied streamwise Fourier mode weights in self-similar coordinates for $k_zh = 14$, 30, 50, 76, 126 ($\lambda_z/h = 0.45$, 0.21, 0.13, 0.08, 0.05 or $\lambda_z^+ = 2327$, 1086, 651, 429, 259): (*a*) streamwise, (*b*) spanwise and (*c*) wall-normal velocity components. Here, the $\widetilde{(\cdot)}$ denotes the weights normalised such that their premultiplied maximum value is one.

Discretisation along the streamwise wavenumber axis was carried out with logarithmic spacing to maintain $\Delta(\ln k_x) \leq 0.05$ or otherwise to align with the DNS streamwise wavenumbers for the smaller values of k_xh, resulting in 132 streamwise Fourier modes being used, and integration performed using the trapezoidal rule along the streamwise wavenumber axis. The optimisation problem was then converted to a standard second-order cone problem and solved with the MOSEK solver (MOSEK ApS 2022). The trend in the optimisation errors, defined by the first term in (2.11*a*), upon increasing the regularisation parameter, was found to increase monotonically with γ (see figure 14 in Appendix A). Hence, γ was set upon inspection of the velocity spectra and smoothness of the weights. An approximate value of $\gamma = 0.5$ was used and changed upon trial and inspection, giving values ranging from 0.3–1.2 across the considered spanwise wavenumbers.

Figure 1 shows solutions to (2.11) for spanwise length scales associated with the logarithmic region, varying from $k_zh = 14$ ($\lambda_z/h \approx 0.45$) up to $k_zh = 126$ ($\lambda_z^+ \approx 259$). Here, the premultiplied weighting is plotted, as this is more physically representative of the forcing spectral density in logarithmic coordinates, as opposed to a weighting correction applied to the velocity spectra. A similar qualitative trend is seen across all components: an approximate self-similarity at relatively large wavelengths ($\lambda_x \gtrsim \lambda_z$) in the weighting, with a spanwise-wavelength-dependent weighting at small wavelengths ($\lambda_x \lesssim \lambda_z$). This trend qualitatively agrees well with the recent finding in Holford *et al.* (2023), where the forcing spectra, obtained for the same linear model, were found to be approximately self-similar at the integral length scale (i.e. $\lambda_x \sim \lambda_z \sim y$), while they are not for $\lambda_x \lesssim \lambda_z$ at which the corresponding DNS spectra are associated with energy cascade. In particular, the forcing spectra for $\lambda_x \lesssim \lambda_z$ were also found to grow with λ_z due to the increased separation of local integral and dissipation length scales, consistent with the behaviours of the weights in figure 1. However, it is important to note that this scale-dependent weighting for $\lambda_x \lesssim \lambda_z$ is of little significance in the modelling of the spectra (Holford *et al.* 2023). At the smaller streamwise length scales of $\lambda_x \lesssim \lambda_z$, large forcing input is required to drive relatively inconsequential features of the velocity spectra associated with the energy cascade (Holford *et al.* 2023) (see the discussion below and figure 2*b*). The contributions of these features to turbulent kinetic energy are small, and they have often been ignored in classical attached eddy models (Townsend 1976; Hwang, Hutchins & Marusic 2022). In a similar context, no attempt is made here to correct or modify the weighting at different

https://doi.org/10.1017/jfm.2023.1073 Published online by Cambridge University Press

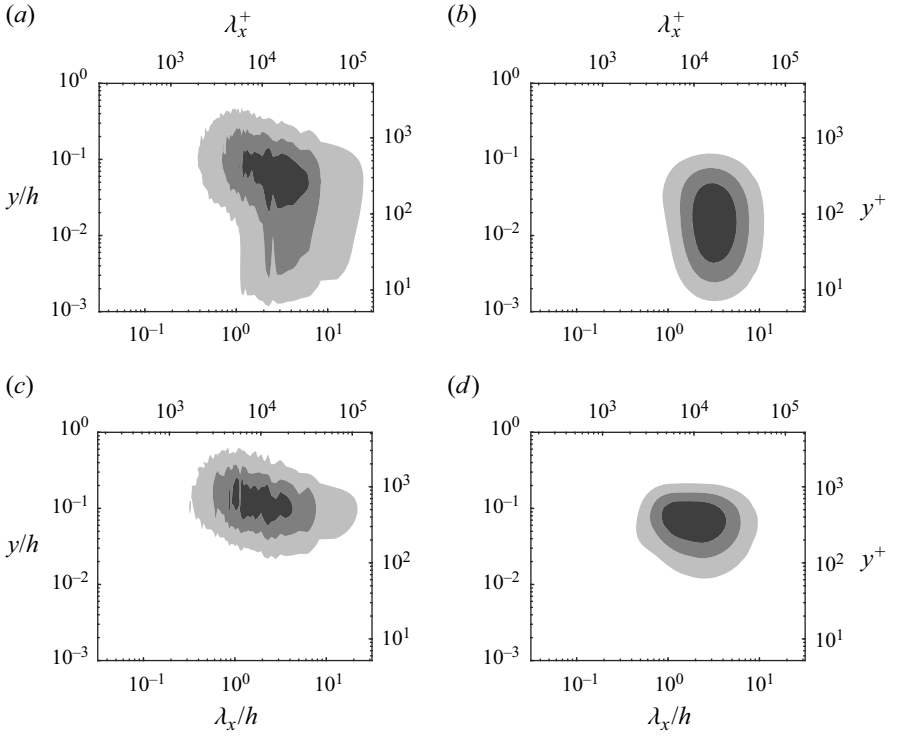

Figure 2. Premultiplied two-dimensional spectra in self-similar coordinates for $k_z h = 14$, $k_z^+ = 0.0027$ ($\lambda_z = 0.45h$, $\lambda_z^+ = 2333$) of (*a*,*b*) streamwise velocity spectra and (*c*,*d*) Reynolds shear stress cospectra determined from (*a*,*c*) DNS and (*b*,*d*) DQLA. The contour levels are separated by 0.25 times the maximum value for each spectra.

length scales. This observation is further confirmed by assuming the weights given from solutions of (2.11) at different λ_z as self-similar and determining the errors between the normalised spectra at different spanwise length scales (see figure 15*d* in Appendix A for the sensitivity to weights). It is shown that the scale-dependent features in the weight of $W_{r,k_x}(k_x/k_z)$ have only a small effect on the structure of the velocity spectra, with the total errors being largely independent of the weight obtained for different k_z in figure 1.

To demonstrate what kind of two-dimensional velocity spectra in the k_x–y plane (2.11) determines, figure 2 compares the streamwise velocity spectra (figure 2*a*,*b*) and Reynolds shear stress cospectra (figure 2*c*,*d*) of the DNS, to the optimally weighted velocity spectra at $k_z h = 14$. In the streamwise component of the optimally weighted spectra (figure 2*b*), an energetic response is seen for $1 \lesssim \lambda_x/h \lesssim 10$, consistent with the DNS streamwise velocity spectra (figure 2*a*). However, the DNS streamwise velocity spectra also have energetic content for $\lambda_x/h \lesssim 1$ away from the wall ($y/h \gtrsim 0.02$). This part of the spectra has been understood to be associated with the physical processes that would not be modelled well by the linearised model (2.1*b*) with (2.2*a*), as discussed in detail in the previous studies (Hwang 2015; de Giovanetti *et al.* 2017; Holford *et al.* 2023). The weighted linear response of leading POD modes appears to neglect a majority of these features. The other qualitative difference between the spectra is the extent to which the primary peak extends towards the wall, with the primary peak from the linear response extending close towards the wall. The observed differences between the DNS streamwise velocity spectra and the optimally weighted leading POD modes indicate some critical limitations in the current

https://doi.org/10.1017/jfm.2023.1073 Published online by Cambridge University Press

modelling approach. It may be overcome by taking the recent approaches designed to fully reconstruct the spectra using the given linear model at a given Reynolds number (Abootorabi & Zare 2023). However, such approaches do not easily enable us to use the modelled spectra for extrapolation to other Reynolds numbers without additional DNS data. For this purpose, a simple approach is taken, and the spectra not directly associated with the linear processes of the flow are ignored. As discussed above, this is similar to the original attached eddy model of Townsend (Townsend 1976), which ignored all the motions related to energy cascade and dissipation (i.e. small-scale detached eddies).

A more substantial qualitative match is found comparing the Reynolds shear stress cospectra (figure 2*c*,*d*). The weighted linear response provides a good agreement for the streamwise wavelength of the primary peak and is overall energetic for a majority of the corresponding DNS spectra. However, the overall amplitude of the Reynolds shear stress generated by the optimally weighted leading POD modes is relatively weak. For the standard L_2-norm over the entire wall-normal distance and considered streamwise wavenumbers (i.e. the root mean square velocities), the ratio of the norms of Reynolds shear stress between the linear model and DNS is approximately 0.4. In contrast, the streamwise response is approximately 0.9, indicating a relatively low Reynolds shear stress. This level of anisotropy is expected to carry through results, an intrinsic limitation in this modelling approach, and it originates from the spatially decorrelated nature of the forcing considered initially (see also Holford *et al.* 2023, for a further discussion). Given that the weight shown in figure 1 is approximately self-similar for $\lambda_x/\lambda_z \gtrsim 1$ and the non-self-similar parts for $\lambda_x/\lambda_z \lesssim 1$ do not generate a strong response for the resulting spectra in figure 2, the weight from $k_z h = 30$ shall be used as a self-similar weight for all wavenumber pairs throughout this study. Note that the choice of the weight does not significantly change the resulting quasi-linear approximation (see Appendix A for the sensitivity to weight choice on results of the entire DQLA procedure at $Re_\tau \approx 5200$).

2.4. *Self-consistent determination of spanwise weighting*

With the self-similar weighting set $W_{r,k_x}(k_x/k_z)$ along the streamwise axis determined, an optimisation problem to determine the spanwise dependent weighting $W_{k_z}(k_z)$ is now considered. As the Reynolds shear stress generated by the fluctuating velocity field must be identical to that required for the mean profile (see also Hwang & Eckhardt 2020, for further details), the following optimisation problem for $W_{k_z}(k_z)$ is further formulated:

$$\min_{W_{k_z}} \left[\frac{\displaystyle\int_0^{2h} (\overline{u'v'}(y) - \mathbb{E}[u'v'](y))^2 Q(y)\,\mathrm{d}y}{\displaystyle\int_0^{2h} (\overline{u'v'}(y))^2 Q(y)\,\mathrm{d}y} \right]^{0.5} + \gamma \left[\int_0^{\infty} \left(\frac{\mathrm{d}^2 W_{k_z}(k_z)}{\mathrm{d}\ln {k_z}^2} \right)^2 R_{uv}(k_z)\,\mathrm{d}k_z \right]^{0.5}, \tag{2.12a}$$

subject to

$$W_{k_z}(k_z) \geq 0, \tag{2.12b}$$

and the values of the weight at the smallest and largest considered spanwise lengths are also constrained to be zero with $W_{k_z}(\lambda_z^+ = 10) = W_{k_z}(\lambda_z = 10h) = 0$. Here, the Reynolds shear stress $\overline{u'v'}(y)$ is given by (2.3) with the assumption that the mean velocity profile is empirically known (e.g. from (2.2*b*) and (2.3)), while the Reynolds shear stress generated by the fluctuation equation (2.1*b*) with the nonlinear term model (2.2*a*) is denoted by

https://doi.org/10.1017/jfm.2023.1073 Published online by Cambridge University Press

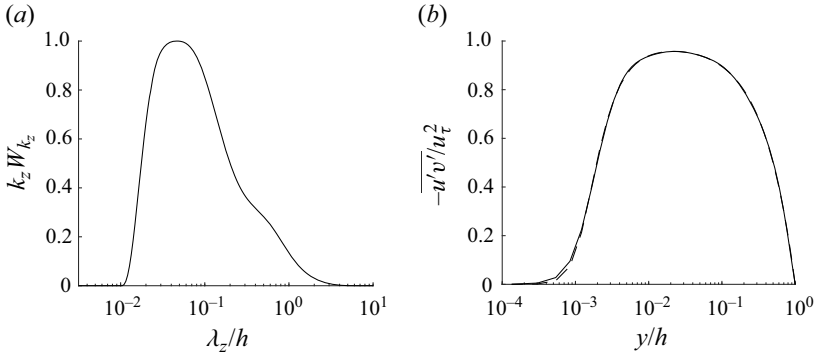

Figure 3. Outputs of quasi-linear approximation optimisation: (*a*) the normalised spanwise weighting of Fourier modes; (*b*) the wall-normal Reynolds shear stress profiles determined from the mean profile (dashed) and the fluctuating components (solid).

$\mathbb{E}[u'v'](y)$ with the definition of

$$\mathbb{E}[u'v'](y) = \frac{1}{4\pi^2}\int_0^{2h}\int_{-\infty}^{\infty}\int_{-\infty}^{\infty} W_{k_z}(k_z) \times \sum_{r=u,v,w} W_{r,k_x}(k_x/k_z)\Phi_{uv,r}^{N_{POD}}(y, y'; k_x, k_z)\delta(y' - y)\,\mathrm{d}k_x\,\mathrm{d}k_z\,\mathrm{d}y'. \quad (2.12c)$$

The optimisation problem in (2.12) is weighted in logarithmic coordinates, such that equal emphasis is placed on logarithmic distance from the wall. The constraint in (2.12*b*) ensures that the velocity covariance operators remain positive definite. Lastly, similar to the determination of the weighting along the streamwise wavenumber axis, a global regularisation term is considered to ensure that the weighting remains smooth, giving a physically reasonable set of velocity spectra. The smoothness regularisation is also weighted by $R_{uv}(k_z)$, where

$$R_{uv}(k_z) = \frac{1}{2\pi}\int_h^{2h}\int_{-\infty}^{\infty}\sum_{r=u,v,w} W_{r,k_x}(k_x/k_z)\Phi_{uv,r}^{N_{POD}}(y, y'; k_x, k_z)\delta(y' - y)\,\mathrm{d}k_x\,\mathrm{d}y'. \quad (2.12d)$$

The $R_{uv}(k_z)$ tends to have large values at large spanwise wavelengths (or small k_z), and this is an outcome of the optimisation problem in (2.11). Since Φ_{uv}^{DNS} contains large energy at large spanwise wavelengths, the regularisation term is more heavily weighted at such wavelengths. This weighting accounts for the rapid decay in the Reynolds shear stress spectra observed in the previous studies (see Skouloudis & Hwang 2021, for a further discussion). It prevents erroneous behaviour in the velocity spectra at larger scales, encouraging a smoothly attached compact support at the large scales (figure 3*a*).

The optimisation problem in (2.12) is discretised and rearranged to a standard form of a second-order cone program and solved with the MOSEK solver. Discretisation along the spanwise wavenumber axis was carried out with logarithmic spacing to maintain $\Delta(\ln(k_z)) \leq 0.05$, with integration performed with the trapezoidal rule. Table 1 shows the number of wavenumbers, collocation points and errors in the Q and L_2 norms of the problem (2.12). Figure 3 shows the weight determined by solving (2.12) and the associated Reynolds shear stress profile compared with $-\overline{u'v'}$. An almost perfect match exists between the two Reynolds shear stress profiles, with the weighting that determines

https://doi.org/10.1017/jfm.2023.1073 Published online by Cambridge University Press

the Reynolds shear stress cospectra to provide a self-consistent approximation. With this procedure established, § 3 compares the results between the DQLA and a DNS (Lee & Moser 2015). The predictive capabilities of the framework are also assessed by using the selected self-similar streamwise weightings as a universal weighting across a range of Reynolds numbers from $Re_\tau = 10^3$ to $Re_\tau = 10^5$ in § 4.

2.5. *Summary*

Thus far, a quasi-linear approximation has been formulated, augmented by DNS data at $Re_\tau \simeq 5200$, combined with the attached eddy hypothesis: i.e. a data-driven quasi-linear approximation. Particular efforts are given such that the model retains a 'predictive' (or 'extrapolative') nature for some of the key turbulence statistics and spectra at any relevant Reynolds numbers (see also §§ 3 and 4) with 'minimal inputs': i.e. a mean velocity profile and a self-similar weight. However, in doing so, a few *ad hoc* assumptions have become unavoidable for the DQLA to retain the 'predictive' nature. In this respect, it would be worth documenting some of its expected characteristics originating from the construction of the model.

(i) Predictability: the main feature of the DQLA is that it is predictable (or extrapolatable) for turbulence statistics and spectra at different Reynolds numbers only with two inputs: a mean profile and a self-similar weight. Note that the mean profile is empirically well documented and commonly available (e.g. Cess 1958), and the self-similar streamwise weight needs to be determined only once at a sufficiently high Reynolds number. By doing so, the DQLA can approach any Reynolds numbers without additional DNS data, as long as the flow remains fully turbulent. Importantly, as is seen in § 4, most of the known Reynolds-number-dependent scaling behaviours of turbulence statistics and spectra appear to be reproduced by the present DQLA. Therefore, it may be a valuable tool for studying turbulence statistics at extremely high Reynolds numbers, where an accurate data set is challenging to obtain, as demonstrated by Skouloudis & Hwang (2021) and § 4.

(ii) Performance: in the DQLA, the first input, a mean profile, is assumed to be known at a given Reynolds number and is determined by an eddy viscosity closure, giving the law of the wall. Given the robustness of the law of the wall, this input should result in reasonable approximations at extremely high Reynolds numbers. The second input used here is the streamwise weighting. The DQLA leverages the self-similar nature of the eddies in the attached eddy hypothesis, focusing on modelling the logarithmic layer. Given the significance of the logarithmic layer grows with Re_τ, the modelling framework should perform best for the high Reynolds numbers, where the features not modelled by this self-similar weight bear a minor significance: e.g. near-wall motions.

(iii) Limitations: the extrapolation capability of the DQLA is, however, obtained at the cost of the accuracy of the resulting turbulence statistics, especially compared with the recent data-driven modelling efforts (Zare *et al.* 2017; Abootorabi & Zare 2023; Holford *et al.* 2023). In particular, the physical processes and the related velocity spectra originating from the original nonlinear term in (2.1*c*) were ignored entirely. However, this is a fundamental limitation of any modelling efforts of turbulent fluctuations based on the linearised Navier–Stokes equations. Even if highly accurate turbulence statistics are obtained with a more accurate forcing incorporating the ignored part of the spectra, the model nonlinear term in (2.2*a*) or any of its variants can only be phenomenological, and they do not have the dynamics

https://doi.org/10.1017/jfm.2023.1073 Published online by Cambridge University Press

of the original nonlinear term in (2.1*c*). Specifically, the velocity components in the DQLA can only give feedback on each other through the one-way coupling of the lift-up effect, i.e. wall-normal velocity, driving the wall-normal vorticity. When considering the fully nonlinear system with time-dependent solutions, the velocity components can interact in other ways: for example, any spanwise shear in the mean velocity will couple the streamwise and spanwise fluctuations, with the latter driving the former in the sense of the lift-up effect. Therefore, the DQLA is a model primarily for turbulence statistics, leveraging the physical processes that the linearised Navier–Stokes equations can depict. In this respect, the models that describe a better turbulent 'dynamics' may be found from some of the recent studies employing more sophisticated state decompositions of the velocity field (e.g. Farrell & Ioannou 2012; Thomas *et al.* 2015; Farrell *et al.* 2016; Hernández *et al.* 2022*a*,*b*). Lastly, the present DQLA employs a steady-state stochastic dynamical systems framework, overlooking any time/frequency domain details. Although the presented framework can be readily extended to encompass the frequency domain using conventional resolvent analysis techniques (Skouloudis & Hwang 2021), introducing this additional time–frequency dimension comes with the trade-off of increased computational overhead or imposing additional constraints and assumptions within the time–frequency domain.

3. Data-driven quasi-linear approximation at $Re_\tau = 5200$

3.1. *One-point turbulence statistics*

The DQLA is initially evaluated at $Re_\tau = 5200$ for comparison with DNS data, as well as to compare the effects of including $k_x \neq 0$ Fourier modes in contrast to the MQLA, which only considers $k_x = 0$ Fourier modes. The MQLA has been re-evaluated using the optimisation problem (2.12), with $\mathbb{E}[u'v']$ determined for streamwise uniform modes ($k_x = 0$). Figure 4 plots the root mean square (r.m.s.) velocity fluctuations and Reynolds shear stress profiles for the DNS, DQLA and MQLA. The Reynolds shear stress profiles are almost identical in logarithmic coordinates (figure 4*d*; see also table 1), indicating that the optimisation problem (2.12) has been successfully implemented for the DQLA and MQLA. The models show the same qualitative features and compare well with DNS, although the streamwise velocity profile lacks a well-defined plateau. The DQLA r.m.s. velocity profiles show a greater degree of consistency with the DNS profiles than the MQLA (figure 4*a–c*) in terms of anisotropy. For instance, $(u'_{rms,max}/w'_{rms,max},\, u'_{rms,max}/v'_{rms,max})$ is approximately (1.82, 2.67), (1.84, 3.48) and (5.78, 13.9) in the DNS, DQLA and MQLA, respectively, with a strong agreement between the DNS and DQLA ratios for the wall-parallel velocity components, due to the inclusion of $k_x \neq 0$ modes.

This mismatch in the MQLA is evidently due to considering only $k_x = 0$ Fourier modes. For the $k_x = 0$ case, the wall-normal derivative of wall-normal velocity fluctuations must be balanced solely by the spanwise variation in the spanwise velocity spectra, given the form of the continuity equation: i.e.

$$\frac{\partial \hat{v}'}{\partial y} + \mathrm{i}k_z\hat{w}' = 0. \tag{3.1}$$

Hence, the spanwise velocity can be determined directly from the wall-normal velocity, itself determined solely from the Orr–Sommerfeld equation. Note that the Orr–Sommerfeld equation for the wall-normal velocity is not coupled with the streamwise

https://doi.org/10.1017/jfm.2023.1073 Published online by Cambridge University Press

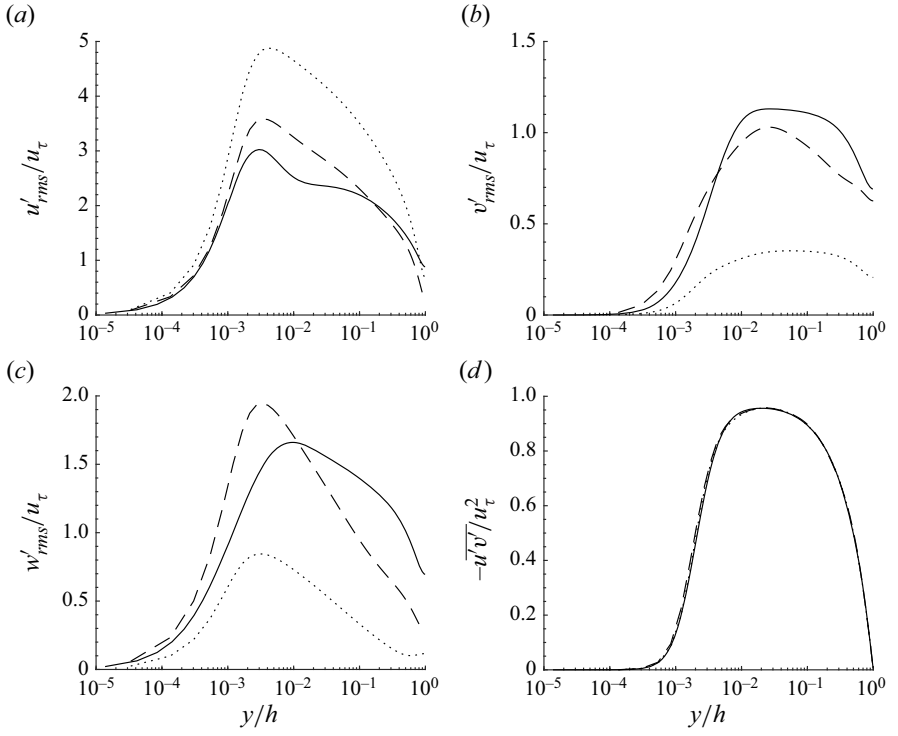

Figure 4. Comparison between DNS at $Re_\tau = 5186$ (solid), DQLA (dashed) and MQLA (dotted) at $Re_\tau = 5200$. (*a*) Streamwise, (*b*) wall-normal and (*c*) spanwise root mean square velocity and (*d*) Reynolds shear stress profiles.

and spanwise velocity. Similarly, when $k_x = 0$, the streamwise momentum equation is only passively coupled with the other two momentum equations through the wall-normal velocity: i.e.

$$\frac{\partial \hat{u}'}{\partial t} + \hat{v}'\frac{\mathrm{d}U}{\mathrm{d}y} = \frac{\mathrm{d}\nu_T}{\mathrm{d}y}\hat{u}' + \nu_T \Delta_{y,z}\hat{u} + \hat{f}'_u, \tag{3.2}$$

where $\Delta_{y,z} = \partial_{yy} - k_z^2$. This momentum equation is the only one that contains the mean shear, which is the source of energy production in the linearised fluctuation equations. When only $k_x = 0$ Fourier mode is considered for velocity fluctuations, as in the MQLA, there is no way to transfer the energy produced by the mean shear at the streamwise velocity component to the other two components. This leads to an overestimation of the streamwise-to-spanwise/wall-normal r.m.s. velocity ratios in the MQLA. By allowing for $k_x \neq 0$ modes in the DQLA, the streamwise momentum equation is now connected to the equations for the other two components through continuity and pressure, significantly reducing the odd anisotropy in the r.m.s. velocity profiles observed in the MQLA. Although the ratio of the peaks of the wall-parallel components is quantitatively similar between the DNS and the DQLA, the ratios in the streamwise and wall-normal components are still overestimated in the DQLA. This is likely due to the simple model for the nonlinear term in (2.2*a*) and the consideration of only two leading POD modes for the construction of velocity spectra.

https://doi.org/10.1017/jfm.2023.1073 Published online by Cambridge University Press

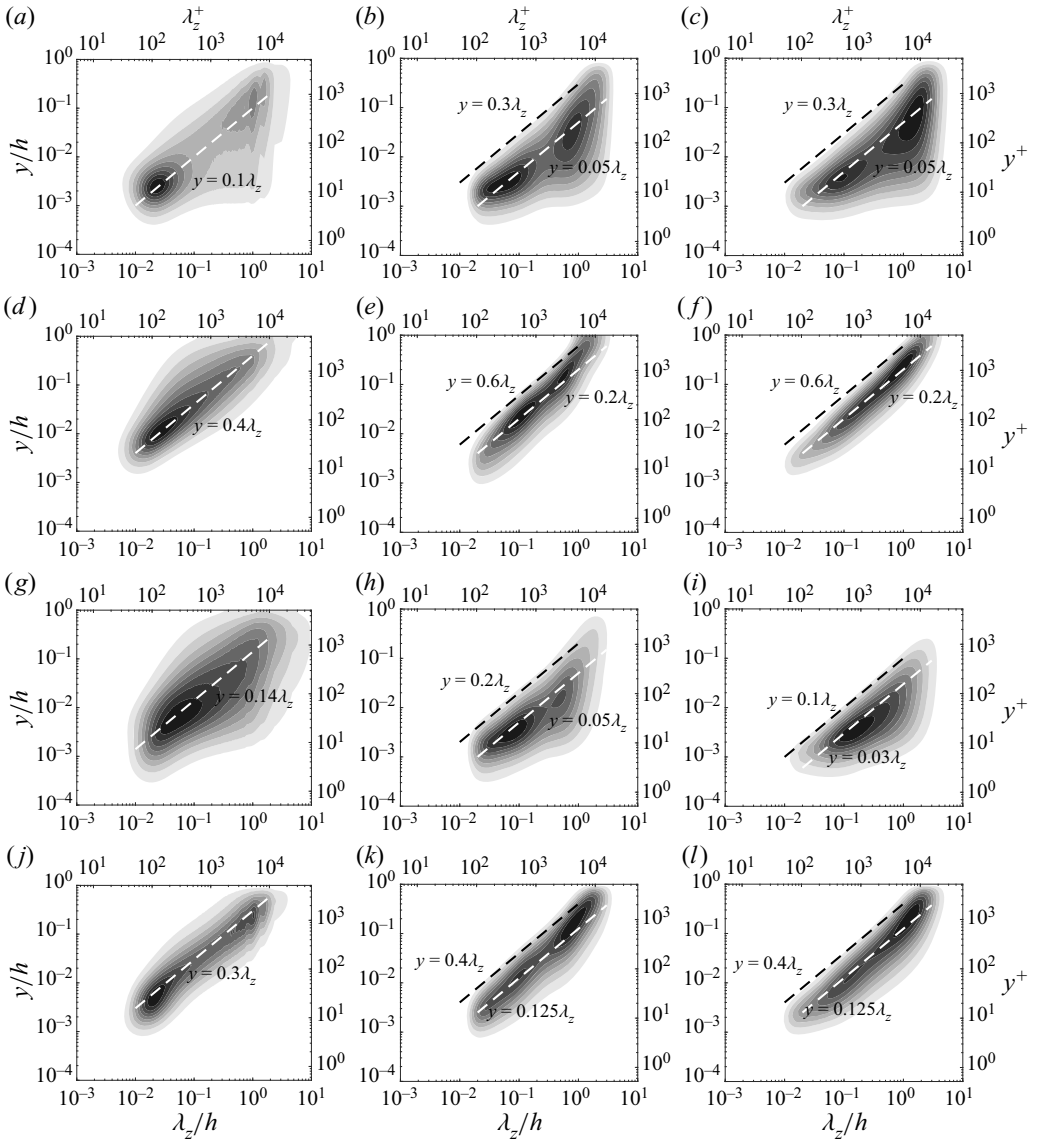

Figure 5. Premultiplied spanwise wavenumber spectra from (*a*,*d*,*g*,*j*) DNS at $Re_\tau = 5186$, (*b*,*e*,*h*,*k*) the DQLA and (*c*,*f*,*i*,*l*) the MQLA at $Re_\tau = 5200$: (*a–c*) streamwise velocity; (*d–f*) wall-normal velocity; (*g–i*) spanwise velocity; (*j–l*) Reynold shear stress. The contours are normalised by 0.1 times the maximum value.

3.2. *One-dimensional spectra*

Figure 5 compares the spanwise one-dimensional velocity spectra from DNS with those of the DQLA and MQLA. Both the MQLA and DQLA compare similarly with the DNS spectra, with all components energetic on a single linear ridge (white dashed lines), as linear ridge in which the energy sharply drops off. In general, the MQLA and DQLA are more energetic closer to the wall. This is most noticeable in the spanwise velocity spectra (figure 5*d–f*), with similar trends in the other components. The DNS spanwise spectra are energetic along $y \approx 0.14\lambda_z$, as opposed to $y \approx 0.03\lambda_z$ in the MQLA. This is partially

https://doi.org/10.1017/jfm.2023.1073 Published online by Cambridge University Press

alleviated in the DQLA, which is energetic farther away from the wall ($y \approx 0.05\lambda_z$), and, at the larger length scales ($\lambda_z/h \approx 1$), the DQLA spectra extend much closer to the channel centreline, more in line with the DNS spectra. Moreover, the energy drops along $y \approx 0.2\lambda_z$ in the DQLA, whereas in the MQLA, this occurs along $y \approx 0.1\lambda_z$, which is below the energy-containing ridge present in the DNS. The qualitative peak locations are also well replicated by the MQLA and DQLA, with a bimodal structure in the streamwise and Reynolds shear stress spectra and a near-wall peak in the spanwise spectra. However, the relative strength of the outer peak in the MQLA and DQLA is consistent with the lack of a well-defined plateau in the streamwise r.m.s. velocity profile. In the DQLA and MQLA, the outer peak remains relatively strong for much of the linear ridge, penetrating the logarithmic region. This leaves only a small region of separation for $y/h \approx 10^{-2}$, compared with the DNS, which has a more diffuse outer peak and a better-defined plateau in the spectra for $y/h \approx 0.01$–0.05. The wall-normal velocity spectra of the MQLA and DQLA contain peaks at much larger length scales than the DNS, at around $y/h \approx 0.1$ and $y/h \approx 0.02$ for the DQLA and MQLA, respectively. Aside from the response along the linear energetic ridges, both wall-parallel velocity spectra exhibit wall-attached features, consistent with the attached eddy hypothesis. Both DQLA and MQLA wall-parallel velocity spectra for $\lambda_z/h \gtrsim 0.1$ penetrate the near-wall region to below $y^+ \lesssim 100$, where the wall-normal velocity spectra are not energetic due to the boundary condition. However, these attached features in the DQLA and MQLA are relatively more energetic than their DNS counterparts.

Overall, the MQLA and DQLA are qualitatively similar when comparing the overall structure of the one-dimensional spanwise wavenumber velocity spectra. This reduces down to the limitations/expectations of the model. Given both the DQLA and MQLA use the same linearised system, they should accurately capture the linearised dynamics present in the real flow, i.e. production. The production in reality (as observed in DNS) consists largely of streaky elongated motions ($k_x/k_z \lesssim 0.1$; see also Lee & Moser 2019), and the $k_x = 0$ approximation employed in the MQLA is not completely unrealistic at least for the production spectra. This is presumably why improvements in the DQLA extension are relatively modest compared with the MQLA.

Figure 6 compares one-dimensional velocity and Reynolds shear stress spectra between DNS and DQLA, excluding the MQLA due to the $k_x = 0$ simplification. In figure 6(*a*,*b*), the streamwise velocity spectra are compared. Good qualitative agreement is observed for long streaky features along the $y = 0.01\lambda_z$ linear ridge. Although the spectra from the DNS suffer from the finite streamwise domain considered, the DQLA replicates large-scale attached structures, albeit with more significant energetic content. The DQLA shows a primary peak at slightly larger length scales ($\lambda_x^+ \approx 2000$) compared with DNS ($\lambda_x^+ \approx 1000$). A distinct separation between the outer and inner peaks is lacking in DQLA, resulting in a negligible plateau and the lack of a distinct outer peak in the streamwise wavenumber spectra. The most significant difference lies above the $y \approx 0.1\lambda_x$ linear ridge, where the DQLA's energetic content drops to zero, while DNS exhibits another energetic linear ridge ($y = 0.35\lambda_x$), strongly correlated with the wall-normal and spanwise velocity fields (see also figure 6*c*,*e*) (for a detailed discussion, see Hwang 2015).

Figure 6(*c*,*d*) compares the wall-normal velocity spectra. There is a good qualitative agreement between the spectra with respect to the energy-containing motions, with a single linear ridge occurring in both at the same approximate length scale, $y \sim 0.35\lambda_x$ and $y \sim 0.30\lambda_x$ in the DNS and DQLA, respectively. The main qualitative difference is the DNS velocity spectra are more energetic above the linear ridge than the DQLA. In the DNS spectra, the contour lines with low levels for $y > 0.8\lambda_x$ do not follow any linear

https://doi.org/10.1017/jfm.2023.1073 Published online by Cambridge University Press

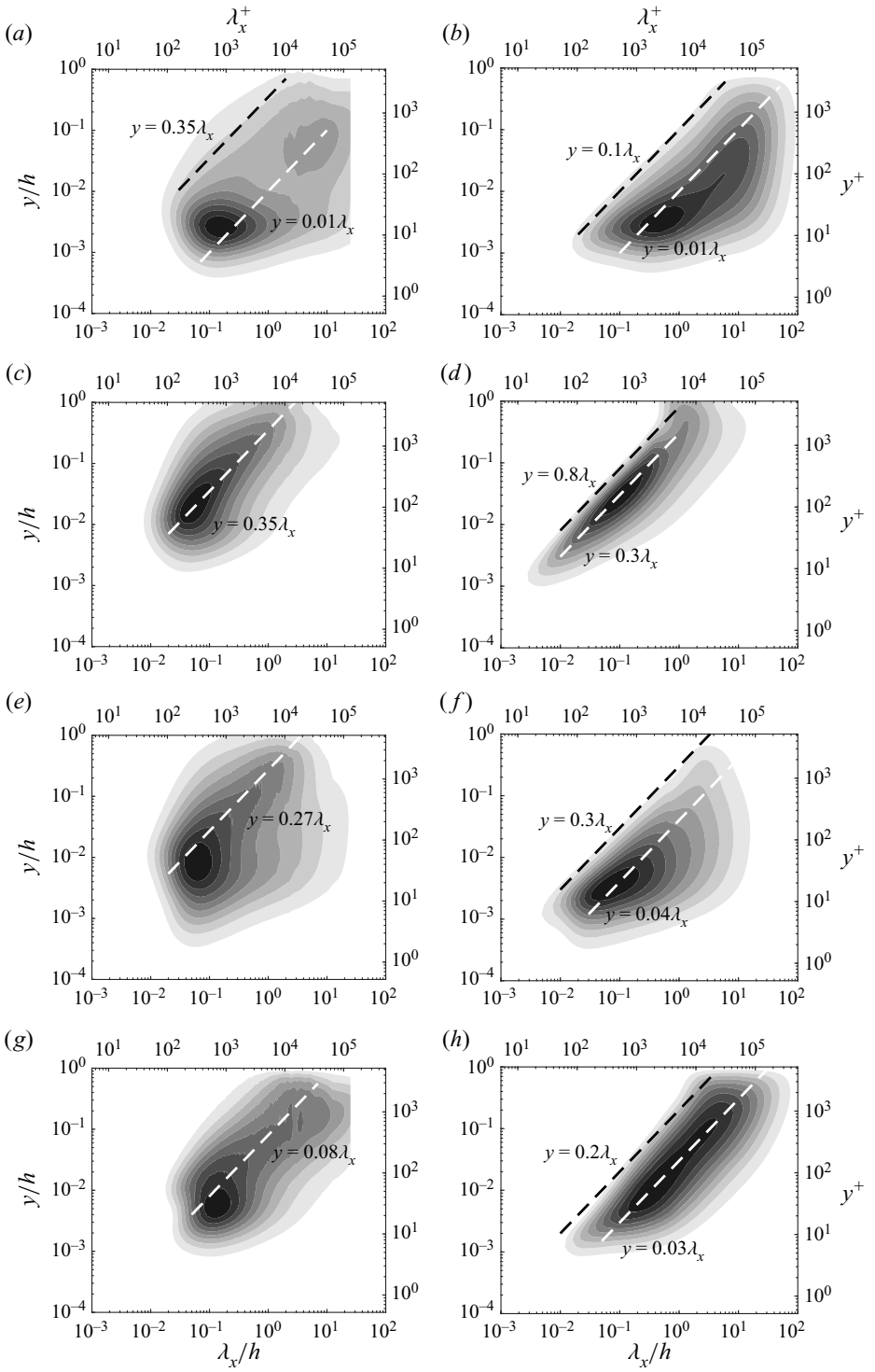

Figure 6. Premultiplied streamwise wavenumber spectra from (*a*,*c*,*e*,*g*) DNS at $Re_\tau = 5186$ and (*b*,*d*,*f*,*h*) the DQLA at $Re_\tau = 5200$: (*a*,*b*) streamwise velocity spectra; (*c*,*d*) wall-normal velocity spectra; (*e*,*f*) spanwise velocity spectra; (*g*,*h*) Reynolds shear stress spectra. The contours are normalised by 0.1 times the maximum value.

https://doi.org/10.1017/jfm.2023.1073 Published online by Cambridge University Press

scaling like $y \sim \lambda_x$, and this part has previously been associated with energy cascade developing a $k_x^{-5/3}$ spectrum (e.g. Agostini & Leschziner 2017). This is expected, given the determination of the self-similar streamwise weighting effectively removed features associated with the energy cascade, as well as the POD filtering process used. Similarly to the spanwise one-dimensional velocity spectra, the primary peak in the DQLA occurs at larger length scales than the DNS. The wall-normal velocity spectra in the DQLA also fall off at a slower rate below this primary peak when compared with the DNS. The low-level contours in the DQLA follow the linear ridge, extending to $y^+ \approx 1$ for $\lambda_x^+ \approx 2$, whereas the DNS extends to $y^+ \approx 1$ for $\lambda_x^+ \approx 100$. This discrepancy in peak location and the DQLA extending to the near-wall region for small streamwise length scales is presumably from the use of a self-similar weighting across all length scales and is likely contributing to the overprediction in the near-wall wall-normal velocity intensity profile and Reynolds shear stress profile. The spanwise velocity spectra are compared in figure 6(*e*,*f*), with the DQLA spectra exhibiting similar characteristics to the streamwise velocity spectra from the DQLA (figure 6*b*). The DQLA model predicts the location of the near-wall peak in the streamwise direction, albeit at a slightly larger length scale ($\lambda_x^+ \sim 500$ in the DQLA compared with $\lambda_x^+ \sim 300$). Most notably, the main energetic regions in the spectra are much closer to the wall than in the DNS. The DNS velocity spectra indicate that the main energy-containing regions are along $y \sim 0.27\lambda_x$. In the DQLA, this appears to be absent. The Reynolds shear stress spectra are compared in figure 6(*g*,*h*), with the main observations consistent with the comparisons of the streamwise and wall-normal velocity spectra. The Reynolds shear stress spectra generated by the DQLA are energetic closer to the wall when compared with the DNS and, similar to the wall-normal velocity spectra, extend along the linear ridge to smaller length scales when compared with DNS, leading to a slight overprediction in the Reynolds stress profile (figure 4*d*).

3.3. *Two-dimensional spectra*

The two-dimensional streamwise velocity spectra and Reynolds shear stress cospectra for a fixed wall-normal location in the near-wall and logarithmic layers are shown in figures 7 and 8, respectively. The attached footprints of the energy-containing eddies from the log and outer regions are most clearly observed for the near-wall location ($y^+ \approx 15$ in figure 7). Comparing the DNS and DQLA spectra in the near-wall region (figure 7), there is a strong qualitative agreement, with the DQLA replicating all the features in the DNS. There is a near-wall primary peak in all the spectra, with the inactive (i.e. Reynold shear stress absent; Townsend 1976) footprints of the eddies present as an approximate linear ridge in the streamwise spectra. Consistent with the previous discussion, the attached footprint is more energetic than that present in the DNS, with the 0.30 contour describing the attached footprint in the DQLA and only the 0.10 contour in the DNS spectra. Since these features in the DQLA are modelled by the eddy viscosity diffusion operator (Hwang 2016; Symon *et al.* 2022), this indicates a more accurate form of eddy viscosity profile in the fluctuating velocity model is required to model these features more accurately. These two-dimensional spectra also show why the peak in the streamwise r.m.s. velocity is overpredicted in the DQLA (figure 4*a*) – the attached footprints of the energy-containing eddies from the log and outer regions contribute relatively more to this integrated quantity over the k_x–k_z plane.

The two-dimensional streamwise velocity spectra and Reynolds shear stress cospectra at a wall-normal location in the log layer are compared in figure 8. At this wall-normal location, the DNS and DQLA spectra are in good agreement for the main energy-containing features, with all of the spectra having a peak occurring at

https://doi.org/10.1017/jfm.2023.1073 Published online by Cambridge University Press

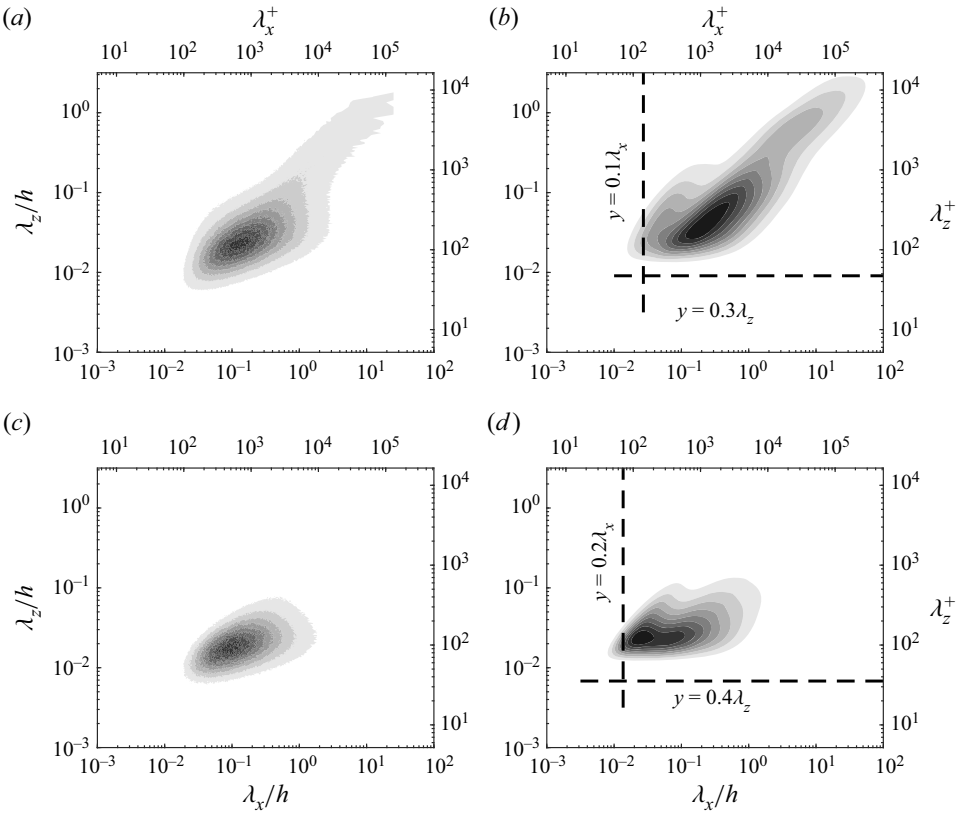

Figure 7. Premultiplied two-dimensional wavenumber spectra at $y^+ \approx 15$ from (*a*,*c*) DNS at $Re_\tau = 5186$ and (*b*,*d*) the DQLA at $Re_\tau = 5200$: (*a*,*b*) streamwise velocity spectra; (*c*,*d*) Reynolds shear stress cospectra. The contours are normalised by 0.1 times the maximum value.

approximately the same length scales. Here, the effects of neglecting energy cascade features are most evident, with the black dashed lines on the DQLA spectra from the linear cutoff lines on the one-dimensional spectra (see figures 5 and 6). Outside these cutoff lines, there is negligible energetic content in the DQLA, whereas no simple linear cutoff was present in the DNS (figures 5 and 6). The DNS spectra are more energetic for the smaller length scales ($\lambda_x \lesssim 3y$, $\lambda_z \lesssim 3y$), which are associated with energy cascade to small scales for dissipation. The contribution of these energy cascade features to the turbulence intensities is expected to be reasonably small.

4. Scaling behaviour up to $Re_\tau = 10^5$

4.1. *Spectra*

The DQLA built from the DNS data at $Re_\tau \approx 5200$ is now repeated for Reynolds numbers ranging from $Re_\tau = 10^3$ to $Re_\tau = 10^5$, given its modelling scope to extrapolate to other Reynolds numbers. Using the self-similar weight $W_{k_x}(k_x/k_z)$ constructed with the DNS data at $Re_\tau \approx 5200$, the weight is interpolated/extrapolated to the considered wavenumber domain at other Reynolds numbers, for which the self-consistent determination of the spanwise weight can be performed, solving (2.12). Firstly, the Reynolds scaling of the one-dimensional spectra is compared between the DNS and DQLA for $Re_\tau \approx 1000$, 2000,

https://doi.org/10.1017/jfm.2023.1073 Published online by Cambridge University Press

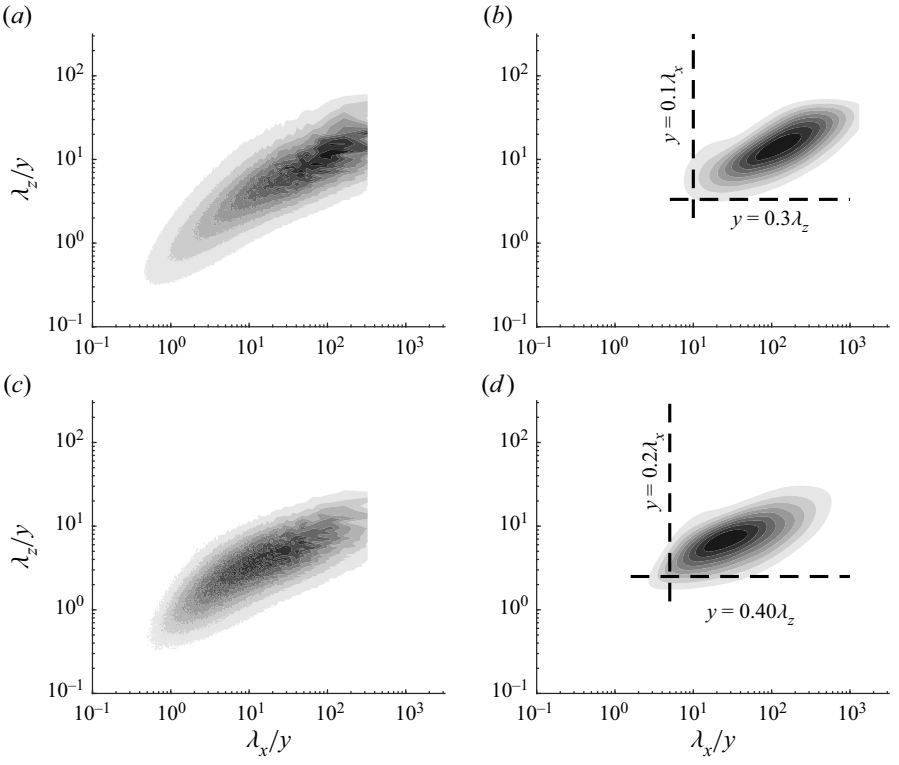

Figure 8. Premultiplied two-dimensional wavenumber spectra at $y^+ \approx 400$ ($y/h \approx 0.075$) from (*a*,*c*) DNS at $Re_\tau = 5186$ and (*b*,*d*) the DQLA at $Re_\tau = 5200$: (*a*,*b*) streamwise velocity spectra; (*c*,*d*) Reynolds shear stress cospectra. The contours are normalised by 0.1 times the maximum value.

5200. The qualitative scaling behaviour in the DQLA is found to be identical to the MQLA in the spanwise one-dimensional spectra and is not displayed here (see Hwang & Eckhardt 2020; Skouloudis & Hwang 2021, for a more complete discussion). There is a strong qualitative agreement between them, with the DQLA and DNS exhibiting inner-scaling features for $O(10) \lesssim \lambda_z^+ \lesssim O(10^3)$ and outer-scaling behaviour for $\lambda_z \approx O(h)$. The attached footprints in the wall-parallel velocity spectra from the DQLA importantly exhibit inner-scaling behaviour (Hwang 2016). Overall, the spanwise velocity spectra are consistent with the attached eddy hypothesis, with qualitative corrections due to the incorporation of viscous effects at a finite Reynolds number (Skouloudis & Hwang 2021).

The outer- and inner-scaled streamwise one-dimensional spectra are shown in figures 9 and 10, respectively. Note that, due to the peak in the wall-normal velocity spectra occurring at logarithmic streamwise length scales in the DQLA, the contour levels for the inner-scaled streamwise one-dimensional spectra for the wall-normal velocity (figure 10*d*) are chosen to follow absolute values rather than normalised ones to exhibit the inner-scaling behaviour. Despite the differences between the spectra at a single Reynolds number, as described in § 3, the scaling behaviour in the DQLA compares very well with the DNS. All the spectra are energetic, spanning from $\lambda_x^+ = O(10^2)$ up to $\lambda_x/h = O(10)$. Both the velocity and Reynolds shear stress spectra have an inner-scaling near-wall peak, with the outer part of the spectra scaling well in outer units. Like the spanwise one-dimensional spectra (Hwang & Eckhardt 2020; Skouloudis & Hwang 2021), the

https://doi.org/10.1017/jfm.2023.1073 Published online by Cambridge University Press

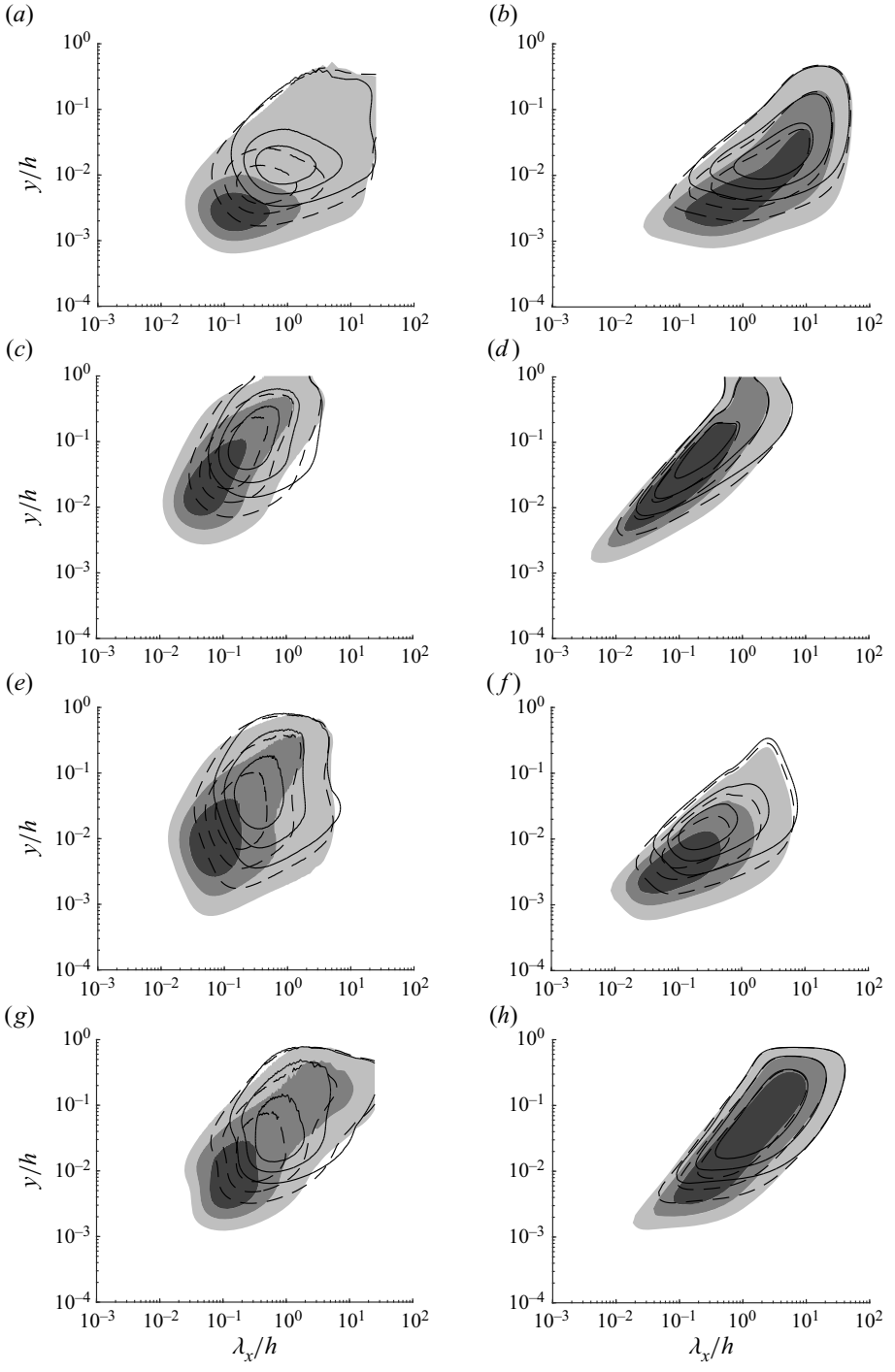

Figure 9. Outer-scaled streamwise one-dimensional spectra from (*a*,*c*,*e*,*g*) DNS (Lee & Moser 2015) and (*b*,*d*,*f*,*h*) the DQLA: (*a*,*b*) streamwise velocity; (*c*,*d*) wall-normal velocity; (*e*,*f*) spanwise velocity; (*g*,*h*) Reynolds shear stress. Here $Re_\tau \simeq 5200$, 2000, 1000 for the shaded, dashed, and solid line contours, respectively. The contour levels are chosen to be 0.25, 0.50 and 0.75 times the maximum value for comparison, except in (*d*) where all contours levels are given by 0.25, 0.50 and 0.75 times the maximum value of the $Re_\tau = 5200$ spectra.

https://doi.org/10.1017/jfm.2023.1073 Published online by Cambridge University Press

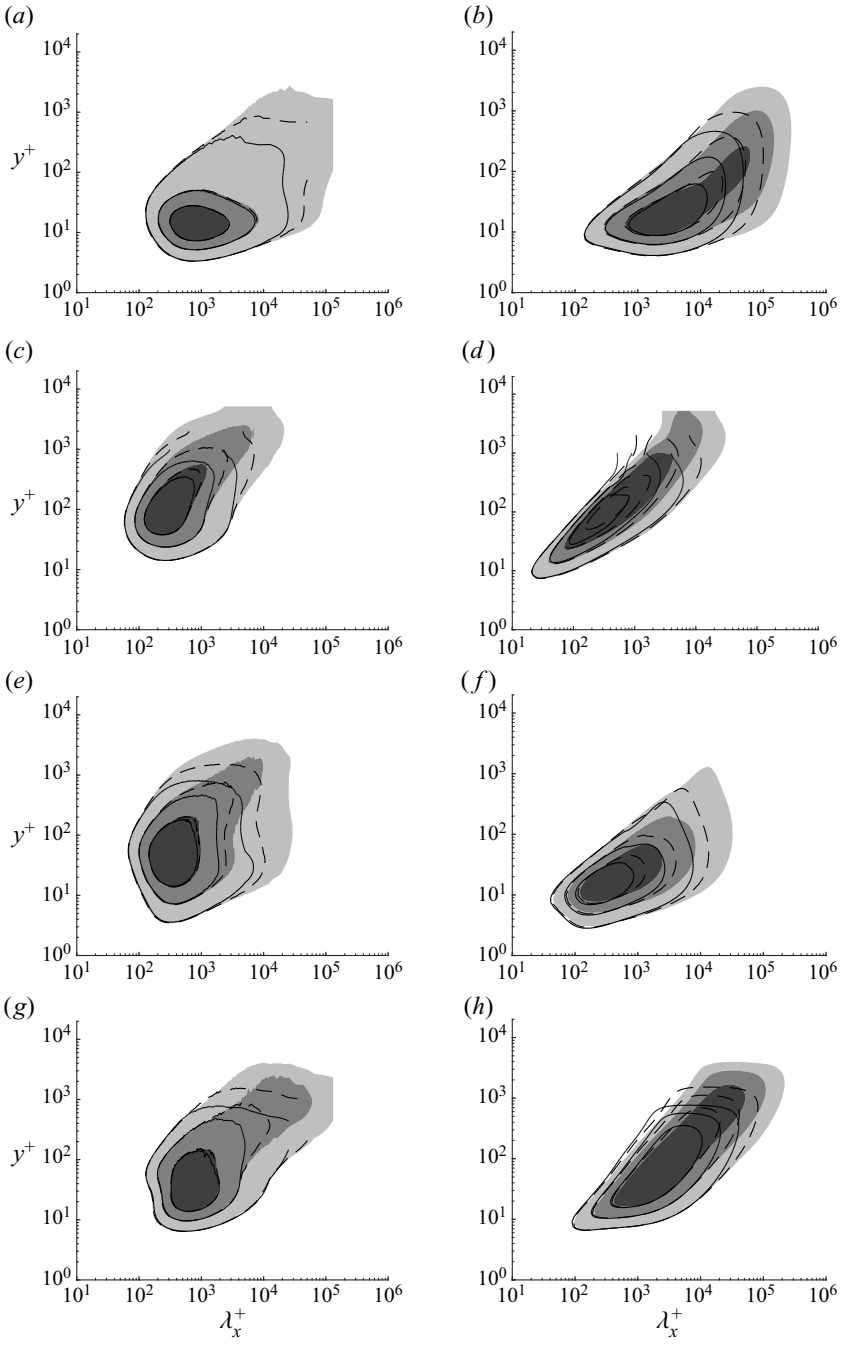

Figure 10. Inner-scaled streamwise one-dimensional spectra from (*a*,*c*,*e*,*g*) DNS (Lee & Moser 2015) and (*b*,*d*,*f*,*h*) the DQLA: (*a*,*b*) streamwise velocity; (*c*,*d*) wall-normal velocity; (*e*,*f*) spanwise velocity; (*g*,*h*) Reynolds shear stress. Here $Re_\tau \approx 5200$, 2000, 1000 for the shaded, dashed and solid line contours, respectively. The contour levels are chosen to be 0.25, 0.50 and 0.75 times the maximum value for comparison, except in (*d*) where all contours levels are given by 0.25, 0.50 and 0.75 times the maximum value of the $Re_\tau = 5200$ spectra.

https://doi.org/10.1017/jfm.2023.1073 Published online by Cambridge University Press

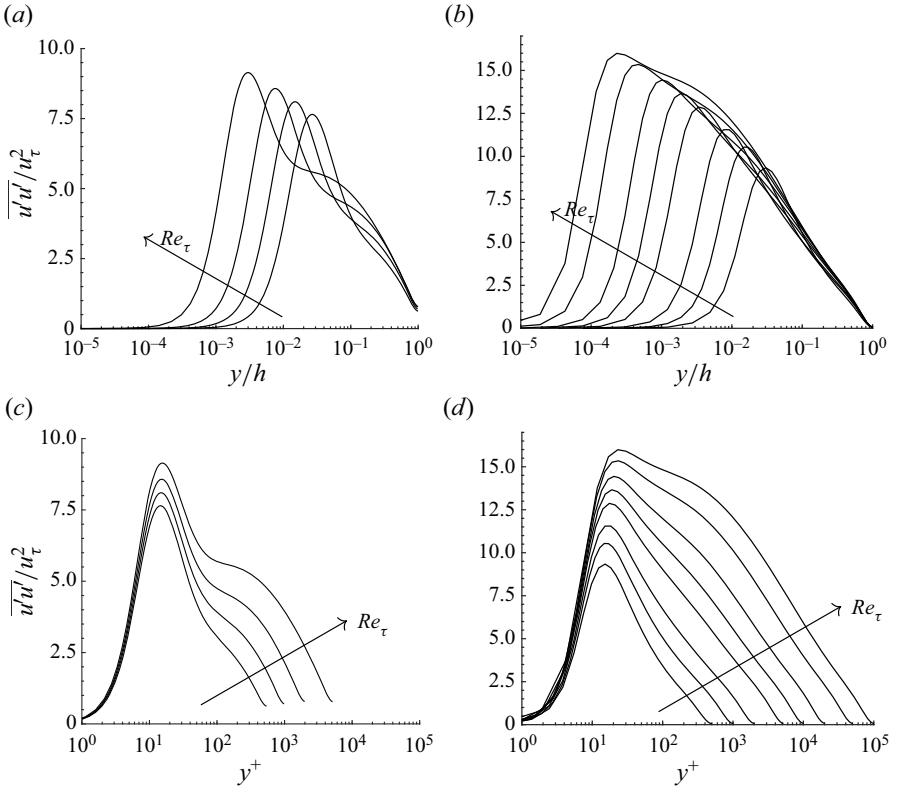

Figure 11. Streamwise turbulence intensity profiles from (*a*,*c*) DNS (Lee & Moser 2015) and (*b*,*d*) the DQLA in (*a*,*b*) outer-scaled coordinates and (*c*,*d*) inner-scaled coordinates. Here, $Re_\tau = 550$, 1000, 1994, 5185 for DNS and $Re_\tau = 500$, 1000, 2000, 5200, 10 000, 20 000, 50 000, 100 000 for the DQLA.

wall-parallel velocity spectra have an attached footprint, scaling well in outer and inner units.

4.2. *Turbulence intensity*

The predictive capabilities of the DQLA are now used up to $Re_\tau = 10^5$, with the focus on the streamwise turbulence intensity profiles. The other components are consistent with the MQLA (Hwang & Eckhardt 2020), albeit with a reduced level of anisotropy, as presented in § 3. The profiles are plotted in the inner- and outer-scaled coordinates in figure 11. The scaling behaviour of the streamwise intensity profiles in DNS and DQLA share the same key features: a near-wall peak at $y^+ \approx 15$ at relatively low Reynolds numbers ($Re_\tau \lesssim 5000$) and an approximate logarithmic decay when scaled in outer units. This behaviour is more evident in the DQLA for $Re_\tau \gtrsim 5200$. For these larger Reynolds numbers, the streamwise intensity profile is consistent with Hwang *et al.* (2022), in which the spectrum-based attached eddy model of Perry *et al.* (1986) was extended for finite Reynolds numbers with an experimental data of Samie *et al.* (2018). In the upper logarithmic layer (or inertial sublayer) from $y^+ = 3.6Re_\tau^{0.5}$ up to $y/h = 0.2$, this model yields the following form of streamwise turbulence intensity

$$\frac{\overline{u'u'}}{u_\tau^2} = -A(Re_\tau)\ln(y/h) + B(Re_\tau), \tag{4.1a}$$

https://doi.org/10.1017/jfm.2023.1073 Published online by Cambridge University Press

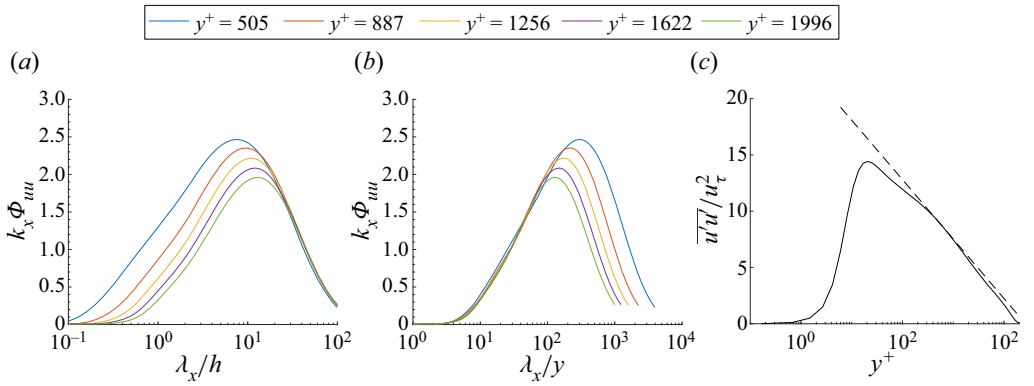

Figure 12. Premultiplied streamwise one-dimensional spectra at various wall-normal locations for $Re_\tau = 20\,000$ in (*a*) outer-scaling coordinates λ_x/h and (*b*) logarithmic coordinates λ_x/y and (*c*) the streamwise turbulence intensity profile (solid) with the attached eddy hypothesis approximation following Hwang *et al.* (2022).

where

$$A(Re_\tau) = A_0 + A_1(Re_\tau). \tag{4.1b}$$

Here, $A(Re_\tau)$ and $B(Re_\tau)$ are supposed to be constants in the limit of infinite Re_τ, and they vary slowly with Re_τ at finite Re_τ (Hwang *et al.* 2022).

An essential prerequisite of the model in Hwang *et al.* (2022) is the existence of y- and h-scaling regions of one-dimensional spectra in the upper logarithmic layer. Figure 12(*a*,*b*) shows that the DQLA successfully reproduces such spectra in the upper logarithmic layer (compare with figure 3(*a*,*b*) in Hwang *et al.* 2022) like the experimental data of Samie *et al.* (2018). Following Hwang *et al.* (2022), $A(Re_\tau)$ and $B(Re_\tau)$ in (4.1*a*) are subsequently approximated from the spectra at all Reynolds numbers

$$A(Re_\tau) = \left[\ln\left(\frac{a_{x,u}}{y}\right) - \ln\left(\frac{a_{x,l}}{h}\right)\right]^{-1} \int_{\ln(a_{x,l}/h)}^{\ln(a_{x,u}/y)} \frac{k_x\Phi_{uu}(k_x, y/h)}{u_\tau^2}\,\mathrm{d}\ln(k_x), \tag{4.2a}$$

$$B(Re_\tau) = A(Re_\tau)\ln\left(\frac{a_{x,u}}{a_{x,l}}\right). \tag{4.2b}$$

Here, $a_{x,u}$ and $a_{x,l}$ are dimensionless constants associated with the upper and lower limits of the integration of the streamwise spectra. However, they have to be chosen through inspection of figure 12(*a*,*b*), they must be 'constants' for all Reynolds numbers. The approximation (4.2) reduces down to using the mean-value theorem to approximate the spectra across these upper and lower limits, with the mean value, or in this case, the Townsend–Perry constant $A(Re_\tau)$, consisting of a universal component A_0 and a viscous correction $A_1(Re_\tau)$. Hence, the upper and lower limits lie at values where the spectra scale in outer (λ_x/h) and logarithmic (λ_x/y) coordinates, respectively. After trial and improvement of the fitting procedure, the upper and lower limits are set with $a_{x,u} = \pi$ and $a_{x,l} = 4\pi/3$, with the comparison of the approximation and streamwise turbulence intensity profile shown in figure 12(*c*).

Table 2 reports the values of $A(Re_\tau)$ and $B(Re_\tau)$ obtained. Consistent with the growing trend of $A(Re_\tau)$ and $B(Re_\tau)$ observed in Hwang *et al.* (2022) with the experimental data from Samie *et al.* (2018), their values obtained from the DQLA data also slowly grow. Importantly, their growth rate tends to be smaller on increasing Re_τ from table 2, indicating

https://doi.org/10.1017/jfm.2023.1073 Published online by Cambridge University Press

$Re_\tau \times 10^{-4}$	0.52	1	2	5	10
$A(Re_\tau)$	2.12	2.21	2.31	2.41	2.47
$B(Re_\tau)$	0.61	0.64	0.67	0.69	0.71

Table 2. The Reynolds-number-dependent model constants for the streamwise turbulence intensity determined following Hwang *et al.* (2022).

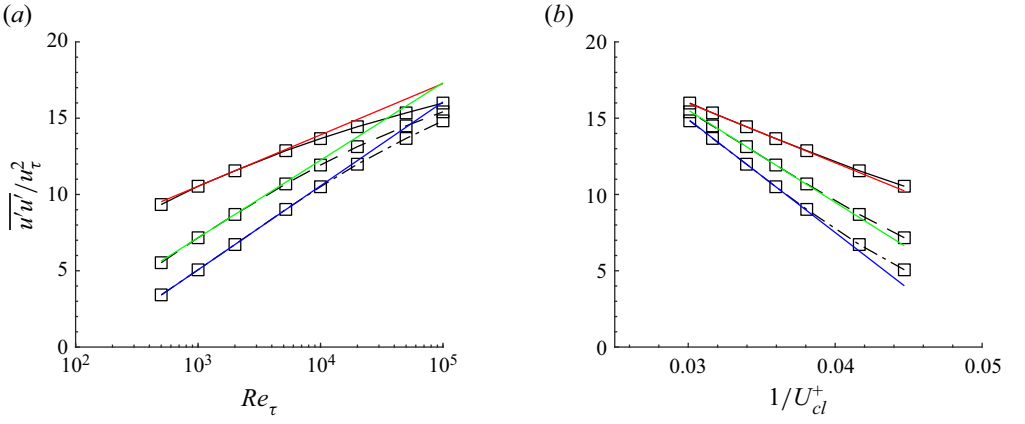

Figure 13. The Reynolds-scaling behaviour of the streamwise turbulence intensity based on (*a*) $\log Re_\tau$ and (*b*) inner-scaled centreline velocity U_{cl}^+. The wall-normal locations correspond to the peak (solid); $y^+ = 50$ (dashed); $y^+ = 100$ (dash-dotted). The coloured lines correspond to (*a*) $\overline{u'u'}/u_\tau^2 = a_1 + b_1 \ln(Re_\tau)$ fitted in the range $Re_\tau = 1000$–2000 and (*b*) $\overline{u'u'}/u_\tau^2 = a_2 + b_2/U_{cl}^+$ fitted in the range $Re_\tau = 20\,000$–$50\,000$.

that they would reach constant values. This trend is consistent with the theoretical model of Hwang *et al.* (2022), which becomes identical to the classical attached eddy model in the limit of $Re_\tau \to \infty$ (Townsend 1976; Perry & Chong 1982; Perry *et al.* 1986).

Apart from the agreement between the near-wall peak and logarithmic decay, the DQLA still does not have a clear plateau behaviour for $y^+ \approx 200$, although one starts to emerge for $Re_\tau \gtrsim 20\,000$. This is likely due to the overly energetic response of the large-scale motions present in the current model, as discussed in § 3. In the DQLA, the primary near-wall peaks are much less distinct than those in the DNS, with the outer-scaling parts of the spectra and their attached features remaining relatively more energetic in the spectra. One possible improvement on the current DQLA framework to account for this plateau would be an outer and inner correction to the streamwise wavenumber weighting. However, this would detract from the predictability of the current framework, with the inner and outer scaling of the corrections having to be prescribed as additional inputs. Another reason for the lack of the plateau is likely due to the particular use of the eddy viscosity profile, with the large-scale response being generally overly energetic. Given how the viscosity of the eddy is used in modelling the attached large-scale features (Hwang 2016; Symon *et al.* 2022; Holford *et al.* 2023), the eddy viscosity profile could perhaps be tuned to replicate these features more carefully, but this is beyond the scope of this study.

Finally, figure 13 shows the scaling behaviour of the near-wall peak and two other inner-scaling locations, $y^+ = 50$, 100. Like the MQLA (Hwang & Eckhardt 2020; Skouloudis & Hwang 2021) in figure 13(*a*), the DQLA shows the deviation of near-wall intensities from the classical logarithmic scaling predicted by an extension of the original

https://doi.org/10.1017/jfm.2023.1073 Published online by Cambridge University Press

attached eddy model (Marusic & Kunkel 2003): i.e. $\overline{u'u'}/u_\tau^2 \sim \ln Re_\tau$. Instead, consistent with the recent findings from a variant of the MQLA (Skouloudis & Hwang 2021), the near-wall streamwise intensities are inversely proportional to the inner-scaled centreline velocity, with the coloured lines given by fits of

$$\frac{\overline{u'u'}}{u_\tau^2} = C - D/U_{cl}^+, \tag{4.3}$$

favouring the prediction made by Monkewitz & Nagib (2015) for a turbulent boundary layer using an asymptotic expansion of near-wall turbulence statistics. Notably, the MQLA (Skouloudis & Hwang 2021) and DQLA provided the same scaling associated with $1/U_{cl}^+$. However, their construction is quite different, especially in that of the full velocity spectra. This suggests that the scaling behaviour of (4.3) is inherently from the linearised Navier–Stokes equations in (2.1*b*) with the model nonlinear term (2.2*a*) rather than a peculiar feature emerging from the construction of the quasi-linear approximation. It also strongly indicates that there must exist a mathematical structure underpinning (4.3). Considering that the DQLA effectively reproduces the scaling behaviour of the streamwise velocity in the upper logarithmic layer, this result warrants thoughtful consideration and should not be underestimated. Importantly, there is growing evidence that the scaling of $\overline{u'u'}/u_\tau^2 \sim \ln Re_\tau$ from the classical attached eddy model may not be valid, as the original attached eddy model is built by ignoring the viscous effect in the near-wall region. In this respect, it is worth mentioning an alternative proposed by the recent work by Chen & Sreenivasan (2021), where a scaling proportional to $Re_\tau^{-1/4}$ was proposed instead of $1/U_{cl}^+$ scaling. Such scaling may fit well with the near-wall streamwise turbulence intensity of DQLA. However, it was recently shown that, in practice, only a negligibly small difference has been found between the $1/U_{cl}^+$ and $Re_\tau^{-1/4}$ scalings upon increasing the Reynolds number (Nagib, Monkewitz & Sreenivasan 2022). To the best of the authors' knowledge, the correct scaling behaviour of the near-wall streamwise turbulence intensity is currently an issue of debate. One of the authors of the present study (Hwang 2022) makes an ongoing effort to address this issue thoroughly in the future.

5. Summary

The MQLA (Hwang & Eckhardt 2020) has been extended in the present study by including streamwise variations of turbulence spectra. To extend the MQLA while still maintaining its predictive nature, self-similarity was used to determine the statistical structure of the forcing. By using the universal nature and growing significance of the logarithmic layer on increasing Reynolds number, a set of self-similar weights was determined by matching the two-dimensional spectra with respect to the streamwise wavenumber and wall-normal location at a single spanwise wavenumber of the linearised Navier–Stokes equations to those of a DNS performed at $Re_\tau \approx 5200$. By reconstructing the velocity spectra from the leading POD modes of the linearised Navier–Stokes equations, the two-dimensional spectra generated reasonably well replicated the DNS spectra. In doing so, the energy cascade-associated features in the spectra were neglected, in line with the attached eddy hypothesis, for the model to be extrapolatable to other Reynolds numbers. From this self-similar weighting with respect to the streamwise wavenumber, the self-consistent determination of the Reynolds shear stress was implemented following Hwang & Eckhardt (2020), completing the DQLA framework.

The DQLA allows complete determination of the two-dimensional velocity spectra and all subsequent statistics, with results compared between the MQLA, DQLA, and DNS. It

https://doi.org/10.1017/jfm.2023.1073 Published online by Cambridge University Press

was shown that the DQLA offers significant quantitative improvements compared with the MQLA with respect to the wall-normal and spanwise r.m.s. velocity profiles. In particular, it significantly reduces the anisotropy in the turbulence intensities while providing the streamwise wavenumber spectra, the scaling of which is consistent with that of DNS. While the DQLA did improve turbulence statistics and spectra compared with the MQLA, there were still some qualitative differences between the DQLA and DNS results. This was demonstrated most clearly in the streamwise one-dimensional spectra, the intensity of which was much stronger than that of the DNS in the region close to the wall while lacking the energetic content at length scales associated with the nonlinear processes modelled in this study (e.g., the streak instability (or transient growth) and energy cascade Schoppa & Hussain 2002; de Giovanetti *et al.* 2017; Doohan *et al.* 2021; Lozano-Durán *et al.* 2021). Aside from the qualitative differences in the spectra, the DQLA framework was shown to retain the predictive capabilities of the MQLA with the scaling behaviour of turbulence intensities and spectra in qualitative agreement with the DNS. In particular, it offers a scaling behaviour consistent with the recent theoretical model of Hwang *et al.* (2022), where the spectrum-based attached eddy model in Perry *et al.* (1986) was extended for finite Reynolds numbers. Also, like the MQLA, the near-wall peak turbulence intensity was inversely proportional to the inner-scaled centreline mean velocity, deviating from the classical prediction based on the attached eddy model.

Acknowledgements. J.H. is supported by Doctoral Training Partnership (DTP) scholarship from the Engineering Physical Science Research Council (EPSRC) in the UK. Y.H. gratefully acknowledges the support of the Leverhulme trust (RPG-123-2019) and EPSRC (EP/T009365/1).

Declaration of interests. The authors report no conflict of interest.

Author ORCIDs.
Jacob J. Holford https://orcid.org/0000-0003-1449-7022;
Myoungkyu Lee https://orcid.org/0000-0002-5647-6265;
Yongyun Hwang https://orcid.org/0000-0001-8814-0822.

Appendix A. Sensitivity of optimisation procedure

To select an appropriate value for γ, figure 14 shows a trade-off curve between the regularisation parameter γ and the errors with respect to the $Q-$norm for each of the spectra. As the errors in all of the components are approximately monotonic, the weights were determined by setting $\gamma = 0.5$ and using trial and inspection in varying γ until the streamwise weights and the velocity spectra are sufficiently smooth and in good qualitative agreement with the DNS velocity spectra.

To check the sensitivity of the DQLA to the choice of self-similar streamwise weighting $W_{k_x}(k_x/k_z)$, the DQLA was performed at $Re_\tau \approx 5200$ with the different weights from figure 1. The turbulence intensity profiles are shown in the figure 15(*a–c*). The streamwise turbulence intensity (figure 15*a*) is relatively insensitive to the choice of the streamwise self-similar weight, while both the wall-normal and spanwise intensities (figure 15*b*,*c*) tend to decrease with $k_z h$. The use of the $k_z h = 30$ weight is justified considering here that the wall-normal and spanwise turbulence intensity profiles are much less sensitive for the $k_z h = 14$–50 weight. Since these wavenumbers are mainly associated with the logarithmic layer, where self-similarity is expected to hold, the different weights from solving (2.11*a*) lead to similar results in a DQLA. The sensitivity to the choice of self-similar streamwise weighting $W_{k_x}(k_x/k_z)$ is also examined in figure 15(*d*), where the total errors between the normalised two-dimensional spectra for fixed spanwise length scales are examined using

https://doi.org/10.1017/jfm.2023.1073 Published online by Cambridge University Press

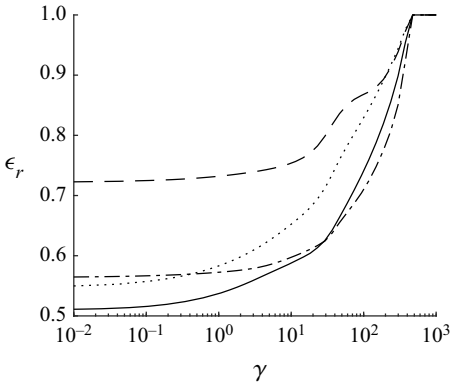

Figure 14. The trade-off curve between the componentwise errors in (2.11*a*), where $\epsilon_r = \|\Phi_r^{DNS} - \Phi_r\|_Q / \|\Phi_r^{DNS}\|_Q$ for $k_z h = 14$ for the streamwise (solid), wall-normal (chain), spanwise velocity spectra (dotted) and Reynolds shear stress cospectra (dashed).

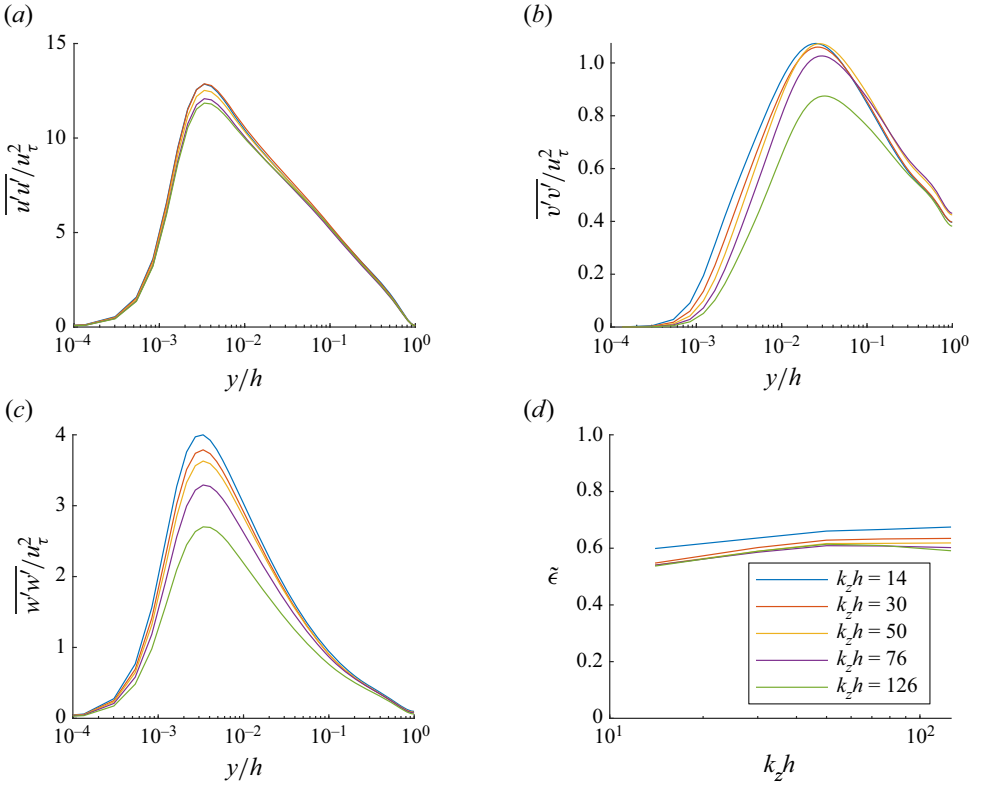

Figure 15. The sensitivity of the DQLA to the choice of streamwise weighting for (*a*) streamwise, (*b*) wall-normal, (*c*) spanwise turbulence intensities; and (*d*) total error in the two-dimensional normalised spectra as defined in (2.11*a*) with the streamwise weighting applied at different $k_z h$. Here, the colour corresponds to the selected $k_z h$ result used for the self-similar streamwise weighting.

https://doi.org/10.1017/jfm.2023.1073 Published online by Cambridge University Press

the weights for different $k_z h$ in figure 1, i.e.

$$\sum_s \left\| \frac{\boldsymbol{\Phi}_s^{DNS}}{\|\boldsymbol{\Phi}_s^{DNS}\|_Q} - \frac{\boldsymbol{\Phi}_s^{DQLA}(W_{r,k_x})}{\|\boldsymbol{\Phi}_s^{DQLA}\|_Q} \right\|_Q , \tag{A1}$$

for $s = \{uu, vv, ww, uv\}$. Figure 15(d) shows that all weights produce a qualitatively similar trend. This justifies the use of the weights as self-similar weights at the other $k_z h$. The normalised spectra produce approximately the same total errors, giving the same approximate statistical structure of the resulting spectra.

References

Abootorabi, S. & Zare, A. 2023 Model-based spectral coherence analysis. *J. Fluid Mech.* **958**, A16.

Agostini, L. & Leschziner, M. 2017 Spectral analysis of near-wall turbulence in channel flow at $Re_\tau = 4200$ with emphasis on the attached-eddy hypothesis. *Phys. Rev. Fluids* **2**, 014603.

del Álamo, J.C. & Jiménez, J. 2006 Linear energy amplification in turbulent channels. *J. Fluid Mech.* **559**, 205–213.

Brandt, L. 2014 The lift-up effect: the linear mechanism behind transition and turbulence in shear flows. *Eur. J. Mech.* B*/Fluids* **47**, 80–96.

Butler, K.M. & Farrell, B.F. 1993 Optimal perturbations and streak spacing in wall-bounded turbulent shear flow. *Phys. Fluids* A*: Fluid Dyn.* **5** (3), 774–777.

Cess, R.D. 1958 A survey of the literature on heat transfer in turbulent tube flow. *Westinghouse Research Rep.* 8-0529.

Chen, X. & Sreenivasan, K.R. 2021 Reynolds number scaling of the peak turbulence intensity in wall flows. *J. Fluid Mech.* **908**, R3.

Chevalier, M., Hœpffner, J., Bewley, T.R. & Henningson, D.S. 2006 State estimation in wall-bounded flow systems. Part 2. Turbulent flows. *J. Fluid Mech.* **552**, 167–187.

Cho, M., Hwang, Y. & Choi, H. 2018 Scale interactions and spectral energy transfer in turbulent channel flow. *J. Fluid Mech.* **854**, 474–504.

Doohan, P., Willis, A.P. & Hwang, Y. 2021 Minimal multi-scale dynamics of near-wall turbulence. *J. Fluid Mech.* **913**, A8.

Ellingsen, T. & Palm, E. 1975 Stability of linear flow. *Phys. Fluids* **18** (4), 487–488.

Farrell, B.F. & Ioannou, P.J. 1992 Stochastic forcing of the linearized Navier–Stokes equations. *Phys. Fluids* A **5** (11), 2600–2609.

Farrell, B.F. & Ioannou, P.J. 2007 Structure and spacing of jets in barotropic turbulence. *J. Atmos. Sci.* **64** (10), 3652–3665.

Farrell, B.F. & Ioannou, P.J. 2012 Dynamics of streamwise rolls and streaks in turbulent wall-bounded shear flow. *J. Fluid Mech.* **708**, 149–196.

Farrell, B.F., Ioannou, P.J., Jiménez, J., Constantinou, N.C., Lozano-Durán, A. & Nikolaidis, M. 2016 A statistical state dynamics-based study of the structure and mechanism of large-scale motions in plane poiseuille flow. *J. Fluid Mech.* **809**, 290–315.

de Giovanetti, M., Sung, H.J. & Hwang, Y. 2017 Streak instability in turbulent channel flow: the seeding mechanism of large-scale motions. *J. Fluid Mech.* **832**, 483–513.

Gupta, V., Madhusudanan, A., Wan, M., Illingworth, S.J. & Juniper, M.P. 2021 Linear-model-based estimation in wall turbulence: improved stochastic forcing and eddy viscosity terms. *J. Fluid Mech.* **925**, A18.

Hall, P. & Sherwin, S.J. 2010 Streamwise vortices in shear flows: harbingers of transition and the skeleton of coherent structures. *J. Fluid Mech.* **661**, 178–205.

Hamilton, J.M., Kim, J. & Waleffe, F. 1995 Regeneration mechanisms of near-wall turbulence structures. *J. Fluid Mech.* **287**, 317–348.

Hernández, C.G., Yang, Q. & Hwang, Y. 2022*a* Generalised quasilinear approximations of turbulent channel flow. Part 1. Streamwise nonlinear energy transfer. *J. Fluid Mech.* **936**, A33.

Hernández, C.G., Yang, Q. & Hwang, Y. 2022*b* Generalised quasilinear approximations of turbulent channel flow. Part 2. Spanwise triadic scale interactions. *J. Fluid Mech.* **944**, A34.

Herring, J.R. 1963 Investigation of problems in thermal convection. *J. Atmos. Sci.* **20** (4), 325–338.

Herring, J.R. 1964 Investigation of problems in thermal convection: rigid boundaries. *J. Atmos. Sci.* **21** (3), 277–290.

Herring, J.R. 1966 Some analytic results in the theory of thermal convection. *J. Atmos. Sci.* **23** (6), 672–677.

https://doi.org/10.1017/jfm.2023.1073 Published online by Cambridge University Press

HŒPFFNER, J., CHEVALIER, M., BEWLEY, T.R. & HENNINGSON, D.S. 2005 State estimation in wall-bounded flow systems. Part 1. Perturbed laminar flows. *J. Fluid Mech.* **534**, 263–294.
HOLFORD, J.J., LEE, M. & HWANG, Y. 2023 Optimal white-noise stochastic forcing for linear models of turbulent channel flow. *J. Fluid Mech.* **961**, A32.
HWANG, Y. 2015 Statistical structure of self-sustaining attached eddies in turbulent channel flow. *J. Fluid Mech.* **767**, 254–289.
HWANG, Y. 2016 Mesolayer of attached eddies in turbulent channel flow. *Phys. Rev. Fluids* **1** (6), 1–18.
HWANG, Y. 2022 Scaling of near-wall streamwise turbulence intensity: from a viewpoint of attached eddy model. *Bull. Am. Phys. Soc.* Z22.00004.
HWANG, Y. & COSSU, C. 2010 Linear non-normal energy amplification of harmonic and stochastic forcing in the turbulent channel flow. *J. Fluid Mech.* **664**, 51–73.
HWANG, Y. & ECKHARDT, B. 2020 Attached eddy model revisited using a minimal quasi-linear approximation. *J. Fluid Mech.* **894**, A23.
HWANG, Y., HUTCHINS, N. & MARUSIC, I. 2022 The logarithmic variance of streamwise velocity and k^{-1} conundrum in wall turbulence. *J. Fluid Mech.* **933**, A8.
ILLINGWORTH, S.J., MONTY, J.P. & MARUSIC, I. 2018 Estimating large-scale structures in wall turbulence using linear models. *J. Fluid Mech.* **842**, 146–162.
JOVANOVIĆ, M. & BAMIEH, B. 2001 Modeling flow statistics using the linearized Navier–Stokes equations. In *Proceedings of the 40th IEEE Conference on Decision and Control (Cat. No.01CH37228)*, vol. 5, pp. 4944–4949.
JOVANOVIĆ, M.R. 2021 From bypass transition to flow control and data-driven turbulence modeling: an input–output viewpoint. *Annu. Rev. Fluid Mech.* **53**, 311–345.
JOVANOVIĆ, M.R. & BAMIEH, B. 2005 Componentwise energy amplification in channel flows. *J. Fluid Mech.* **534**, 145–183.
LEE, M. & MOSER, R.D. 2015 Direct numerical simulation of turbulent channel flow up to $Re_\tau \approx 5200$. *J. Fluid Mech.* **774**, 395–415.
LEE, M. & MOSER, R.D. 2019 Spectral analysis of the budget equation in turbulent channel flows at high Reynolds number. *J. Fluid Mech.* **860**, 886–938.
LOZANO-DURÁN, A., CONSTANTINOU, N.C., NIKOLAIDIS, M.A. & KARP, M. 2021 Cause-and-effect of linear mechanisms sustaining wall turbulence. *J. Fluid Mech.* **914**, 1–58.
LUHAR, M., SHARMA, A.S. & MCKEON, B.J. 2014 Opposition control within the resolvent analysis framework. *J. Fluid Mech.* **749**, 597–626.
MADHUSUDANAN, A., ILLINGWORTH, S.J. & MARUSIC, I. 2019 Coherent large-scale structures from the linearized Navier–Stokes equations. *J. Fluid Mech.* **873**, 89–109.
MALKUS, W.V.R. 1954 The heat transport and spectrum of thermal turbulence. *Proc. R. Soc. Lond.* A *Math. Phys. Sci.* **225** (1161), 196–212.
MALKUS, W.V.R. 1956 Outline of a theory of turbulent shear flow. *J. Fluid Mech.* **1** (5), 521–539.
MANTIČ-LUGO, V., ARRATIA, C. & GALLAIRE, F. 2014 Self-consistent mean flow description of the nonlinear saturation of the vortex shedding in the cylinder wake. *Phys. Rev. Lett.* **113**, 084501.
MANTIČ-LUGO, V. & GALLAIRE, F. 2016 Self-consistent model for the saturation mechanism of the response to harmonic forcing in the backward-facing step flow. *J. Fluid Mech.* **793**, 777–797.
MARSTON, J.B., CHINI, G.P. & TOBIAS, S.M. 2016 Generalized quasilinear approximation: application to zonal jets. *Phys. Rev. Lett.* **116**, 214501.
MARSTON, J.B., CONOVER, E. & SCHNEIDER, T. 2008 Statistics of an unstable barotropic jet from a cumulant expansion. *J. Atmos. Sci.* **65** (6), 1955–1966.
MARUSIC, I. & KUNKEL, G.J. 2003 Streamwise turbulent intensity formulation for flat-plate boundary layers. *Phys. Fluids* **15** (8), 2461.
MCKEON, B.J. & SHARMA, A.S. 2010 A critical-layer framework for turbulent pipe flow. *J. Fluid Mech.* **658**, 336–382.
MONKEWITZ, P.A. & NAGIB, H.M. 2015 Large-Reynolds-number asymptotics of the streamwise normal stress in zero-pressure-gradient turbulent boundary layers. *J. Fluid Mech.* **783**, 474–503.
MORRA, P., NOGUEIRA, P.A.S., CAVALIERI, A.V.G. & HENNINGSON, D.S. 2021 The colour of forcing statistics in resolvent analyses of turbulent channel flows. *J. Fluid Mech.* **907**, A24.
MORRA, P., SEMERARO, O., HENNINGSON, D.S. & COSSU, C. 2019 On the relevance of Reynolds stresses in resolvent analyses of turbulent wall-bounded flows. *J. Fluid Mech.* **867**, 969–984.
MOSEK APS 2022 The MOSEK optimization toolbox for MATLAB manual. Version 10.0.
NAGIB, H., MONKEWITZ, P.A. & SREENIVASAN, K.R. 2022 Reynolds number required to accurately discriminate between proposed trends of peak normal stress in wall turbulence. *Bull. Am. Phys. Soc.* Q13.00006.

https://doi.org/10.1017/jfm.2023.1073 Published online by Cambridge University Press

NOGUEIRA, P.A.S., MORRA, P., MARTINI, E., CAVALIERI, A.V.G. & HENNINGSON, D.S. 2020 Forcing statistics in resolvent analysis: application in minimal turbulent Couette flow. *J. Fluid Mech.* **908**, A32.

PAUSCH, M., YANG, Q., HWANG, Y. & ECKHARDT, B. 2019 Quasilinear approximation for exact coherent states in parallel shear flows. *Fluid Dyn. Res.* **51** (1), 011402.

PERRY, A.E. & CHONG, M.S. 1982 On the mechanism of wall turbulence. *J. Fluid Mech.* **119**, 173–217.

PERRY, A.E., HENBEST, S. & CHONG, M.S. 1986 A theoretical and experimental study of wall turbulence. *J. Fluid Mech.* **165** (-1), 163.

PUJALS, G., GARCÍA-VILLALBA, M., COSSU, C. & DEPARDON, S. 2009 A note on optimal transient growth in turbulent channel flows. *Phys. Fluids* **21**, 015109.

RAN, W., ZARE, A. & JOVANOVIĆ, M.R. 2021 Model-based design of riblets for turbulent drag reduction. *J. Fluid Mech.* **906**, A7.

ROSENBERG, K. & MCKEON, B.J 2019 Efficient representation of exact coherent states of the Navier–Stokes equations using resolvent analysis. *Fluid Dyn. Res.* **51** (1), 011401.

SAMIE, M., MARUSIC, I., HUTCHINS, N., FU, M.K., FAN, Y., HULTMARK, M. & SMITS, A.J. 2018 Fully resolved measurements of turbulent boundary layer flows up to $Re_\tau = 20\,000$. *J. Fluid Mech.* **851**, 391–415.

SCHMID, P.J. & HENNINGSON, D.S. 2001 *Stability and Transition in Shear Flows*, Applied Mathematical Sciences, vol. 142. Springer New York.

SCHOPPA, W. & HUSSAIN, F. 2002 Coherent structure generation in near-wall turbulence. *J. Fluid Mech.* **453**, 57–108.

SKOULOUDIS, N. & HWANG, Y. 2021 Scaling of turbulence intensities up to $Re_\tau = 10^6$ with a resolvent-based quasilinear approximation. *Phys. Rev. Fluids* **6** (3), 034602.

SYMON, S., ILLINGWORTH, S.J. & MARUSIC, I. 2021 Energy transfer in turbulent channel flows and implications for resolvent modelling. *J. Fluid Mech.* **911**, A3.

SYMON, S., MADHUSUDANAN, A., ILLINGWORTH, S.J. & MARUSIC, I. 2022 On the use of eddy viscosity in resolvent analysis of turbulent channel flow. *Phys. Rev. Fluids* **8**, 064601.

THOMAS, V.L., FARRELL, B.F., IOANNOU, P.J. & GAYME, D.F. 2015 A minimal model of self-sustaining turbulence. *Phys. Fluids* **27** (10), 105104.

THOMAS, V.L., LIEU, B.K., JOVANOVIĆ, M.R., FARRELL, B.F., IOANNOU, P.J. & GAYME, D.F. 2014 Self-sustaining turbulence in a restricted nonlinear model of plane Couette flow. *Phys. Fluids* **26** (10), 105112.

TOBIAS, S.M. & MARSTON, J.B. 2013 Direct statistical simulation of out-of-equilibrium jets. *Phys. Rev. Lett.* **110**, 104502.

TOBIAS, S.M. & MARSTON, J.B. 2017 Three-dimensional rotating Couette flow via the generalised quasilinear approximation. *J. Fluid Mech.* **810**, 412–428.

TOWNE, A., LOZANO-DURÁN, A. & YANG, X. 2019 Resolvent-based estimation of space-time flow statistics. *J. Fluid Mech.* **883**, A17.

TOWNSEND, A.A. 1976 *The Structure of Turbulent Shear Flow*, 2nd edn. Cambridge University Press.

WALEFFE, F. 1997 On a self-sustaining process in shear flows. *Phys. Fluids* **9** (4), 883–900.

WEIDEMAN, J.A.C. & REDDY, S.C. 2000 A MATLAB differentiation matrix suite. *ACM Trans. Math. Softw.* **26** (4), 465–519.

ZARE, A., JOVANOVIĆ, M.R. & GEORGIOU, T.T. 2017 Colour of turbulence. *J. Fluid Mech.* **812**, 636–680.

https://doi.org/10.1017/jfm.2023.1073 Published online by Cambridge University Press